

# JGR Solid Earth

## RESEARCH ARTICLE

10.1029/2022JB024272

### Key Points:

- At the last glacial maximum, maximum horizontal stress ranges from  $-16$  to  $40$  MPa from forebulge to flexural trough regions, respectively
- At present, the Fram Strait (between Greenland and Svalbard) is dominantly under E-W oriented tensile maximum horizontal stress ( $\sim -4$  MPa)
- Glacially induced stresses along the forebulge off the Svalbard west-coast could be sufficient to destabilize faults and favor gas seepage

### Correspondence to:

R. Vachon,  
[remi.e.vachon@uit.no](mailto:remi.e.vachon@uit.no)

### Citation:


Vachon, R., Schmidt, P., Lund, B., Plaza-Faverola, A., Patton, H., & Hubbard, A. (2022). Glacially induced stress across the Arctic from the Eemian interglacial to the present—Implications for faulting and methane seepage. *Journal of Geophysical Research: Solid Earth*, 127, e2022JB024272. <https://doi.org/10.1029/2022JB024272>

Received 23 FEB 2022  
Accepted 21 JUN 2022

© 2022. The Authors.

This is an open access article under the terms of the [Creative Commons Attribution License](#), which permits use, distribution and reproduction in any medium, provided the original work is properly cited.

# Glacially Induced Stress Across the Arctic From the Eemian Interglacial to the Present—Implications for Faulting and Methane Seepage

R. Vachon<sup>1</sup> , P. Schmidt<sup>2</sup> , B. Lund<sup>2</sup> , A. Plaza-Faverola<sup>1</sup> , H. Patton<sup>1</sup> , and A. Hubbard<sup>1</sup> 

<sup>1</sup>CAGE-Centre for Arctic Gas Hydrate, Environment, and Climate, Department of Geosciences, UiT The Arctic University of Norway, Tromsø, Norway, <sup>2</sup>Department of Earth Sciences, Geophysics, Uppsala University, Uppsala, Sweden

**Abstract** Strong compressive and shear stresses generated by glacial loading and unloading have a direct impact on near-surface geological processes. Glacial stresses are constantly evolving, creating stress perturbations in the lithosphere that extend significant distances away from the ice. In the Arctic, periodic methane seepage and faulting have been recurrently associated with glacial cycles. However, the evolution of the Arctic glacial stress field and its impact on the upper lithosphere have not been investigated. Here, we compute the evolution in space and time of the glacial stresses induced in the Arctic lithosphere by the North American, Eurasian and Greenland ice sheets during the latest glaciation. We use glacial isostatic adjustment (GIA) methodology to investigate the response of spherical, viscoelastic Earth models with varying lithospheric thickness to the ice loads. We find that the GIA-induced maximum horizontal stress ( $\sigma_H$ ) is compressive in regions characterized by thick ice cover, with magnitudes of 20–25 MPa in Fennoscandia and 35–40 MPa in Greenland at the last glacial maximum. Simultaneously, a tensile regime with  $\sigma_H$  magnitude down to  $-16$  MPa dominates across the forebulges with a mean of  $-4$  MPa in the Fram Strait. At present time,  $\sigma_H$  in the Fram Strait remains tensile with an East-West orientation. The evolution of GIA-induced stresses from the last glaciation to present could destabilize faults along tensile forebulges, for example, the west-coast of Svalbard. A more tensile stress regime as during the Last Glacial Maximum would have more impact on pre-existing faults that favor gas seepage from gas reservoirs.

**Plain Language Summary** The Earth's surface is constantly moving, slowly changing in response to external forces such as the weight of ice sheets that grow and decay during glacial cycles. Although most of the ice from the latest ice age melted long ago, the Earth's surface in and around the previously glaciated region is still responding—rising and falling—which affects the stress regime in the crust. The aim of this study is to quantify the evolution in space and time of the stress perturbation caused by fluctuations in the main ice sheets of the northern hemisphere since the last interglacial—123 ka BP. To achieve our goal, we build a numerical model of the Earth and apply the varying weight of the ice sheets at its surface. Our results show that the perturbation of stress caused by the deformation of the Earth during the last glacial cycle and its aftermath could be sufficient to disturb natural gas reservoirs within oceanic sediments,—such as along Svalbard's western coastline. Understanding the relationship between glacial forcing and methane seepage at Arctic margins is important to advance in the quantification of the effect of such natural phenomena on global climate.

## 1. Introduction

Glacial isostatic adjustment (GIA) describes the mechanical response of the Earth to glacial loading and unloading. This effect is well known in formerly glaciated areas (e.g., Scandinavia, Svalbard and the Barents Sea), and in regions where glaciers are actively retreating (e.g., Greenland, North America, and Antarctica). Depression of the Earth's surface during glacial loading causes flexure of the lithosphere, forming a subsidence bowl under the glaciated area and a peripheral bulge off the ice sheet boundary. This flexural response is important because it generates horizontal stresses of the same magnitude as the vertical stress induced by the weight of the ice cover (Johnston et al., 1998; Kendall et al., 2005; Lund et al., 2009). After the retreat of the ice sheet, the Earth's surface rebounds to gradually reach its equilibrium state, reducing the changes in the local stress field. Whilst the vertical stress closely follows the temporal evolution of the ice-load, the horizontal stresses build up and decay away over significantly longer time spans, depending on the viscosity of the underlying mantle. Hence, over the course of a glaciation and in the aftermaths, the GIA process will contribute deviatoric stresses in the lithosphere. The

magnitude of the Earth's response to the glacial build up and deglaciation depends on several parameters, such as the elastic and rheological composition of the mantle and lithosphere, and the geometry and evolution of the ice sheet (in terms of areal extent and thickness).

GIA modeling is often used to infer sea-level changes caused by glacial loading and unloading (Mitrovica & Milne, 2003), to reconstruct the time and space evolution of ice sheets and to estimate rheological properties of the Earth (e.g., Argus et al., 2014; Cathles, 1972; Lambeck et al., 2010; Lecavalier et al., 2014; Patton et al., 2016; Siegert & Dowdeswell, 2004). Improvements in computational power has led to the development of widely used general-purposed finite element (FE) software that can be adapted to GIA analysis (e.g., Bångtsson & Lund, 2008; Hooper et al., 2011; Schmidt et al., 2012; Spada et al., 2011; Wu, 1992a, 1992b, 2004). Although numerical modeling has been extensively used for GIA problems, only a limited number of publications calculate and discuss the state of stress induced by glacial cycles in de-glaciated or glaciated areas (Ivins, 2003; Jull & McKenzie, 1996; Klemann & Wolf, 1998; Lambeck & Purcell, 2003; Lund et al., 2009; Løtveit et al., 2019; Schmidt et al., 2013; Steffen et al., 2020; Wu et al., 1999). These studies have a particular focus on glacially induced earthquakes associated with major faults on land and the implications for society of the present-day occurrence of glacially induced seismicity in glaciated (e.g., Greenland and Antarctica) or formerly glaciated regions (e.g., Fennoscandia and North America).

GIA modeling allows calculation of paleo-stresses associated with glacial-interglacial transitions. The implications of reconstructing the evolution of glacial stresses extend to offshore Arctic regions where the release of copious amounts of greenhouse gases to the ocean have been associated to glacial dynamics (e.g., Andreassen et al., 2017; Crémière et al., 2016; Himmler et al., 2019; Plaza-Faverola et al., 2011; Portilho-Ramos et al., 2018; Portnov et al., 2016; Wallmann et al., 2006). Although these studies have suggested a close link between glacial-interglacial transitions and seafloor methane emissions, such a link remains poorly understood. Large amounts of methane (i.e., and higher order hydrocarbons) are present at continental margins either as gas hydrates or in the gas phase within the sedimentary cover. Methane is particularly abundant in the Earth's lithosphere because it is generated by both organic (i.e., decomposition of organic matter either by microbes or by high temperatures in buried formations) and inorganic processes related to chemical transformations at ultra-high temperatures within the lithosphere (e.g., Etiope & Sherwood Lollar, 2013). The release of these greenhouse gases into the ocean and the atmosphere is part of the Earth carbon budget (e.g., Etiope et al., 2008; Ruppel & Kessler, 2017). Sedimentary faults and fractures are major pathways for fluids in the shallow strata provided favorable pore fluid pressure conditions (e.g., Hornbach et al., 2004). Transient dynamic stresses associated with faulting may lead to pore pressure increases that lower the effective stress and that in turns promotes more faulting and shearing (e.g., Dugan & Sheahan, 2012). Any external mechanism that alters the local stress regime (e.g., glacial isostasy) will have an effect in the pressure field that controls the timing and magnitude of the gas release (e.g., Ramachandran et al., 2022).

Here, we model for the first time the spatial and temporal evolution of glacial stress in the Barents Sea, Svalbard, the Fram Strait and Greenland through the last 122,800 years, to get a sense of stress field variations through glacial, deglacial and interglacial periods. We pay particular attention to the evolution of glacial stress since the Last Glacial Maximum (LGM) until present day. Our results can allow constraining simulations of fault-controlled methane fluxes at glaciated margins and contributes therefore to the ongoing debate about the relationship between glacial-interglacial transitions and the release of methane at Arctic continental margins.

## 2. Modeling Approach

In this study, we use a finite element approach to model the response of the solid Earth to glacial loading and unloading. This method allows us to include complex 3D structures in our models, such as lateral variations of the elastic thickness of the Earth's lithosphere ( $T_e$ ). Three features are essential when trying to tackle the GIA problem: (a) The implementation of the momentum equation in the modeling code or software, (b) the reconstructions of the ice sheets chosen for the loading conditions of the models, and (c) the geometry and rheology of the Earth model.

### 2.1. Modeling Glacial Isostatic Adjustment With General-Purposed FE Software

Throughout this study, we use the FE approach based on Wu (2004), which allows for the computation of GIA stresses with general-purpose FE packages. The GIA problem is here modeled using the momentum equation for a quasi-static and compressible spherical Earth that is in hydrostatic equilibrium. However, solving the full momentum equation often yields numerical complications. For example, instability of the numerical solution can occur because of the internal buoyancy and pre-stress advection being of the same magnitude but with different signs. Another important challenge arises when including self-gravitation into the model, because this requires solving either the Poisson's (for a compressible material) or the Laplace's equations (for an incompressible material), significantly increasing the computation time. Here we take a first order approach and do not include self-gravitation nor the change in density due to material compression, that is, internal buoyancy, but we do allow for material compressibility (Klemann et al., 2003). It was previously shown that the internal buoyancy and self-gravitation terms yield variations in the vertical displacement solution induced by GIA of less than 5% under the center of the ice load (Schotman et al., 2008). Note that we also do not consider minor processes like gravitational attraction of the evolving ice mass. After simplification, the momentum equation becomes:

$$\nabla \cdot \sigma - \nabla (u \cdot \rho_0 g_0 \hat{r}) = 0 \quad (1)$$

where  $\sigma$  is the stress tensor,  $u$  is the displacement vector,  $\hat{r}$  is a unit vector in the radial direction,  $\rho$  the density and  $g$  the gravitational acceleration. The first term describes the divergence of stress while the second defines the advection of the pre-stress field by the material in motion.

To our knowledge, our study is the first to use the modeling software COMSOL Multiphysics® v6.0 to tackle the GIA problem (COMSOL, 2022). To implement pre-stress advection into COMSOL Multiphysics®, we follow the implementation scheme of Schmidt et al. (2012) for which the authors advocates the use of elastic springs at all density contrasts. We thus set elastic spring foundations at the surface of the model and at each density contrast within the Earth model. The spring constant acts only in the direction of gravity (radial direction).

Our implementation method has been tested against pre-existing GIA solutions and benchmarks (Bångtsson & Lund, 2008; Lund et al., 2009; Spada et al., 2011; Wu, 1992a). Our computation of the vertical displacement and velocity fields yield small differences (less than 5%) compared with the mentioned studies, especially with solutions computed by other commercial FE packages such as Abaqus. The horizontal displacement calculated from our model are generally overestimating solutions from spectral method by 10%–15%.

### 2.2. Model of the Eurasian, Greenland and North American Ice Sheets

One of the two major components in GIA computation is the loading of the ice sheet model. Having a detailed, well-resolved ice reconstruction is a pre-requisite when computing displacements and associated stresses induced by glacial loading. For this study, we include in our GIA model all major ice bodies from the Northern hemisphere (i.e., the Eurasian, Greenland, and North American ice sheets) that could affect the stress regime in the Fram Strait region. To do so, we combine two regional ice reconstructions, namely the UiT\_2021 model, an extended model reconstruction of the Late Weichselian Eurasian ice sheet developed by Patton et al. (2016, 2017) and the Huy3 model from Lecavalier et al. (2014). We chose the UiT\_2021 and Huy3 models for this study because they are respectively the state of the art in the regional reconstruction of the Eurasian and Greenland ice sheets. Parametric studies and comparison with relative sea level (RSL) constraints have shown that each model overall performs well against empirical constraints and other regional or global ice reconstructions, which adds confidence in our usage of the ice models. For example, RSL misfits associated with the last deglaciation (Patton et al., 2017), which remains unmodified in the more recent UiT\_2021 reconstruction, have been directly compared to the recent benchmark study of Auriac et al. (2016), that compared various ice sheet and GIA models against RSL and geodetic constraints around the Barents Sea. Results indicate that the UiT\_2017 improved on previous regional ice-sheet reconstructions, such as Siegert and Dowdeswell (2004) and Näslund (2010). For the Greenland ice sheet, the Huy3 model explains the majority of RSL data around the island, except in Nanortalik where an important misfit exists (Lecavalier et al., 2014). However, recent studies have shown that the misfit between predicted GIA solution and observation in that region was potentially due to tectonic activities (glacially induced faulting and earthquake) during the early Holocene (Steffen et al., 2020). These local reconstructions of the Greenland and Eurasian ice sheets are coupled with the North American part of the global ICE-6G model

from Peltier et al. (2015). We chose the ICE-6G model because of its time range being similar than the Huy3 and UiT\_2021 models. In addition, the ICE-6G model is considered reliable by the GIA community thanks to its global performance against RSL and geodetic constraints (Auriac et al., 2016; Peltier et al., 2015). As our study does not focus on glacial stresses in North America, but rather need to include the ice sheet to simulate far-field conditions, the coarser spatial resolution of the ICE-6G model in comparison to regional reconstructions was considered sufficient for our study. We do not include the Icelandic ice sheet in this study, whose far field effects are not considered significant enough to affect the Fram Strait regions. Note that the three selected ice sheet reconstructions follow the evolution in time of the ice thickness from 122.8 kyrs BP to present but exclude Anthropocene changes. The characteristics of the UiT\_2021, Huy3 and ICE-6G models are described below.

For Northern Europe, we use the ice reconstruction by Patton et al. (2017) (model UiT\_2021) which follows the evolution of the Eurasian ice sheet (Figure 1a) for the last 122.8 kyrs starting from the Eemian interglacial period to the present day. The model is sampled on a  $50 \times 50$  km grid with a temporal resolution of 100 years. The UiT\_2021 reconstruction includes three periods of glaciation with the ice cover reaching a maximum extent at 88.2 kyrs BP, 59.8 kyrs BP and 23 kyrs BP (Figure A1). Figure 1a shows the geometry of the ice model at 23 kyrs BP, with ice covering Northern Europe from the British Isles to the Severnaya Zemlya archipelago. The ice cover reaches a maximum thickness exceeding 2.25 km at two locations: (a) on the northern coast of the Gulf of Bothnia and (b) at the center of the Barents Sea. Each glacial maximum is followed by an almost entire collapse of the ice sheet system. Final deglaciation over Fennoscandia, the Barents Sea and the British Isles occurs 9.7 kyrs BP. Only small patches of ice remain over the northeast of Svalbard during the Holocene.

For the Greenland region, we use the recent ice reconstruction (model Huy3) by Lecavalier et al. (2014) which covers the evolution of the Greenland ice sheet from 122 kyrs BP to present (Figure 1b). The model is sampled on a  $20 \times 20$  km grid with a temporal resolution of 6,000 years between 122 and 32 kyrs BP, 1,000 years between 32 kyrs BP and 17 kyrs BP and 500 years at more recent times. The Huy3 reconstruction is built using a 3D thermomechanical ice sheet model, coupled with a GIA model of sea-level changes, and constrained by past ice extents, past changes in relative sea-level, ice-core derived thinning and the present-day configuration of the Greenland ice sheet. It includes the last three periods of glaciation with glacial maximum at 80, 62, and 16.5 kyrs BP (Figure A1). At 16.5 kyrs BP, the ice sheet is entirely covering Greenland and has a maximum thickness that exceeds 3 km at the center of the island (Figure 1b). At present time, about 55%–60% of the ice volume observed at the 16.5 kyrs BP glacial maximum, remains.

For the North American ice sheet, we crop the global ICE-6G model from Peltier et al. (2015) to only keep the ice bodies that cover north America (Figure 1c). We selected the extended version of the ICE-6G model that is sampled on a  $1^\circ \times 1^\circ$  grid with a temporal resolution of 2 kyrs between 122 and 32 kyrs, and a resolution of 250 years between 32 kyrs and present. The model is built upon successive reconstructions of the last Pleistocene deglaciation, constrained by geological data (i.e., observations of ice sheet margins, relative sea-level curves and global mean sea level curve). It includes the last three glacial-interglacial cycles with glacial maximum at 86, 64, and 26 kyrs BP. At 26 kyrs BP, the maximum ice thickness exceeds 4 km. The last remnants of the ice sheet over North America vanishes 6 kyrs BP. Only small patches of ice remain in Alaska and Canada, which reflects the presence of local glaciers.

Each of the ice sheet models have an individual timing for the LGM. For the rest of the study and specifically in the results section, we refer to the LGM that is based on the Eurasian ice reconstruction, which occurs c. 23 kyrs BP.

We convert the ice thickness data from the three ice reconstructions into a two-dimensional temporally evolving surface load that we apply on top of the viscoelastic Earth. The ice load is calculated as follows:

$$\sigma_{\text{ice}} = T_{\text{ice}} \rho_{\text{ice}} g \quad (2)$$

with  $T_{\text{ice}}$  the ice thickness and  $\rho_{\text{ice}}$  the density of the ice ( $917 \text{ kg} \cdot \text{m}^{-3}$ ).

### 2.3. The Solid FE Earth Models

The second major component in the computation of GIA stresses is the Earth model. For this study, we model the solid Earth using a layered three-dimensional spherical FE model, defined by a Maxwell viscoelastic rheology

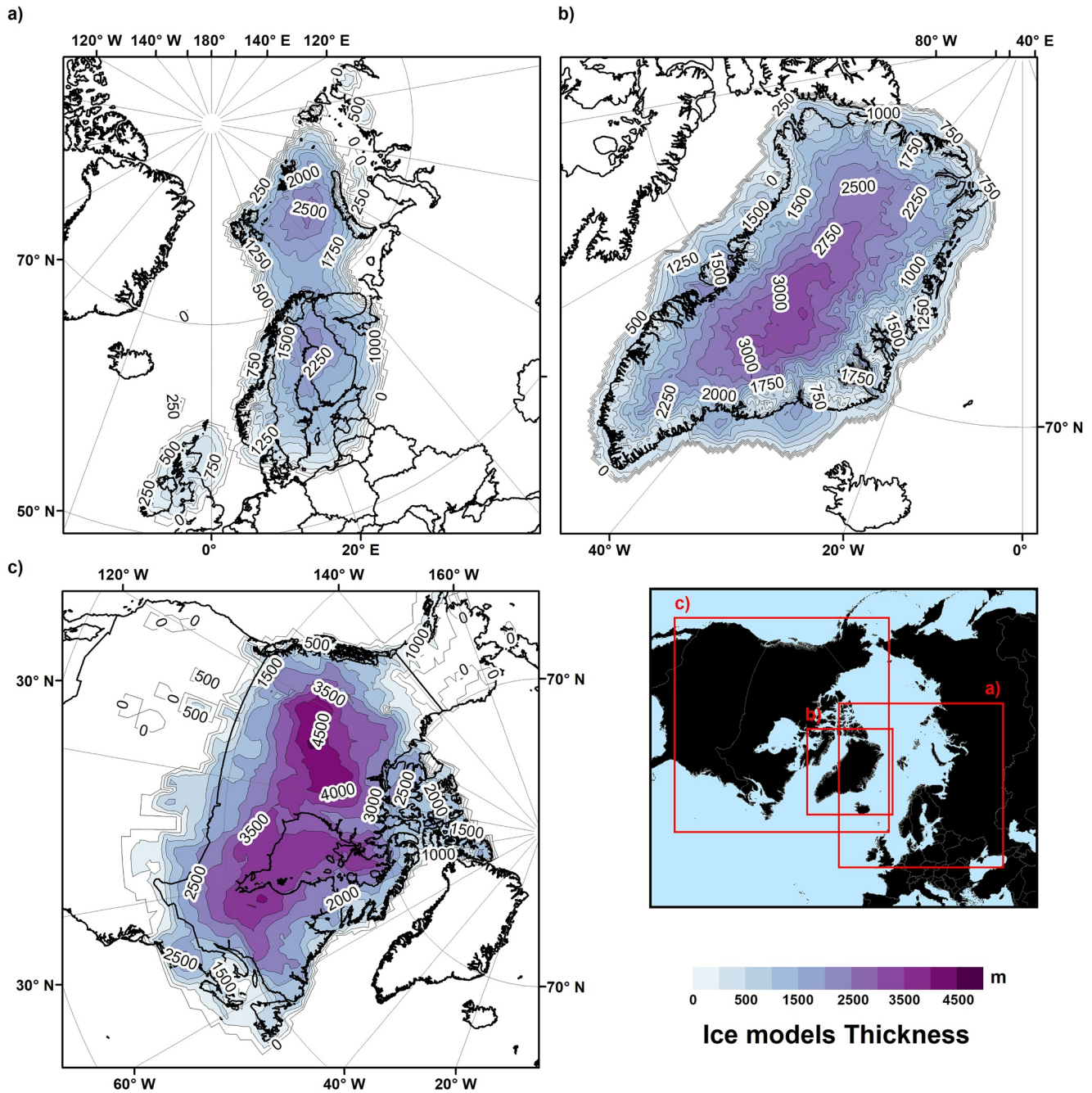


**Figure 1.** Map of the ice thickness for the reconstruction of (a) the North European ice sheet (Patton et al., 2016, 2017), (b) the Greenland ice sheet (Lecavalier et al., 2014) and (c) the North American ice sheet (Peltier et al., 2015), plotted at 23 kyr BP, 16.5 and 28 kyr BP, respectively.

with elastic parameters based on the Preliminary Earth Model (Dziewonski & Anderson, 1981; see Table 1). The choice for the viscosity values of the upper mantle ( $1.5 \times 10^{21}$  Pa.s) and lower mantle ( $1.5 \times 10^{21}$  Pa.s) was based on a local GIA model of Fennoscandia that performs overall well against observational constraints (Schmidt et al., 2014). The model has a radius  $R$  of 6,371 km, but we only model the outer 2,800 km of the Earth, from the surface to the core-mantle boundary (CMB) that is fixed in every direction (Figure 2a). The choice of a fixed boundary condition at the CMB may be questioned. We therefore also tested a model with free-slip boundary conditions at the CMB which yielded less than 0.7% difference in the stress results under the center of the ICE at LGM.

**Table 1**  
*Material Parameters for the GIA Model*

Layer #	Depth [km]	Density $\rho$ [kg.m <sup>-3</sup> ]	Poisson ratio $\nu$	Young modulus E [GPa]	Viscosity $\mu$ [pa.s]
1. Upper Crust	15	2,750	0.28	64	-
2. Lower Crust	50	3,251	0.28	156	-
3. Lower Lithosphere	60; 120; 20–175	3,378	0.28	170	-
4. Upper Mantle 1	410	3,433	0.30	182	$1.5 \times 10^{21}$
5. Upper Mantle 2	670	3,837	0.30	263	$1.5 \times 10^{21}$
6. Lower Mantle	2,800	4,853	0.30	552	$1.5 \times 10^{21}$

*Note.* Elastic parameters are based on the Preliminary Earth Model (Dziewonski & Anderson, 1981).

In this study, we use two types of lithospheric models: (a) Models with constant layer thicknesses and (b) a model that includes lateral variations. For the first type, we build two end members: one model where the base of the lithosphere is located at 60 km depth and a second model where the base is located at 120 km depth. These two end members values are based on a compromise between the best-fitting rheology of the optimum Eurasian and Greenland ice sheet reconstructions presented in Patton et al. (2017) and Lecavalier et al. (2014), respectively. For simplicity, we will refer to these models as TE60 and TE120, respectively. The second type of Earth model includes a lithosphere with a laterally varying thickness (Figure 2c). This model is based on the global lithospheric reconstruction of Tesauro et al. (2013; personal communication). The elastic thickness of the lithosphere ( $T_e$ ) varies from 10 km along the North Atlantic ridge and exceeds 175 km in the cratonic regions of Northern Europe and North America. To avoid geometrical complications in the Earth model, we decided to cut the minimum elastic thickness to 20 km instead of 10 km as such a thin layer would require the addition of finer elements in the model, causing the run time to increase. At present, we do not include a plate boundary in the model. For the rest of the manuscript, we will refer to this model as VL20-175. In every Earth model, the elastic lithosphere and viscoelastic mantle are subdivided into three layers each described by different elastic modulus and thickness (see Table 1).

The Earth model is discretized by a complex mesh network with a resolution that varies as a function of depth, longitude, and latitude. For latitudes north of 45° and longitudes in between -90° and +90°, the finite elements in the elastic lithosphere have a mean node separation of 70 km, against 300 km in the rest of the model (see Figure 2b). In the entire Earth model, the elastic lithosphere is vertically discretized by seven elements, three for the first elastic layer and two each for the second and third elastic layers. For latitudes north of 45° we set the elements to be approximately 150 km thick in the upper mantle and 250 km thick in the lower mantle. In the rest of the model, elements are approximately 300 km thick in the upper mantle and 700 km thick in the lower mantle. In total, the mesh consists of 650,000 quadratic tetrahedral elements, which corresponds to 4,800,000 degrees of freedom. The model runs from 122.8 kyrs BP to present, with a maximum time stepping of 100 years which results in an overall computation time of about 50 hr on a workstation that include an eight cores 3.70 GHz processor.

#### 2.4. Observational Constraints

The lithosphere is affected by many different ongoing processes (e.g., tectonics and mantle dynamics) of which the GIA contribution may not always be a major player and individual components are hard to entangle. Further, stress measurements are sparse and generally from shallow depths. A direct comparison of model predictions of stress to available observations is thus challenging. Therefore, model verification will focus on surface velocities. In this study, we compare our model with GPS data at three key locations: Greenland, Svalbard and Fennoscandia. In Fennoscandia, GIA will be the major contributor to surface deformation, whereas in Greenland and Svalbard, other processes may dominate the signal (e.g., present-day ice mass loss, tectonic forces, mantle upwelling, among others).

For Fennoscandia and its close surroundings, we use the BIFROST2015 data, presented in Kierulf et al. (2021) and processed using the ITRF2008 reference frame (see Figure 3a). Measurements over Fennoscandia reflect

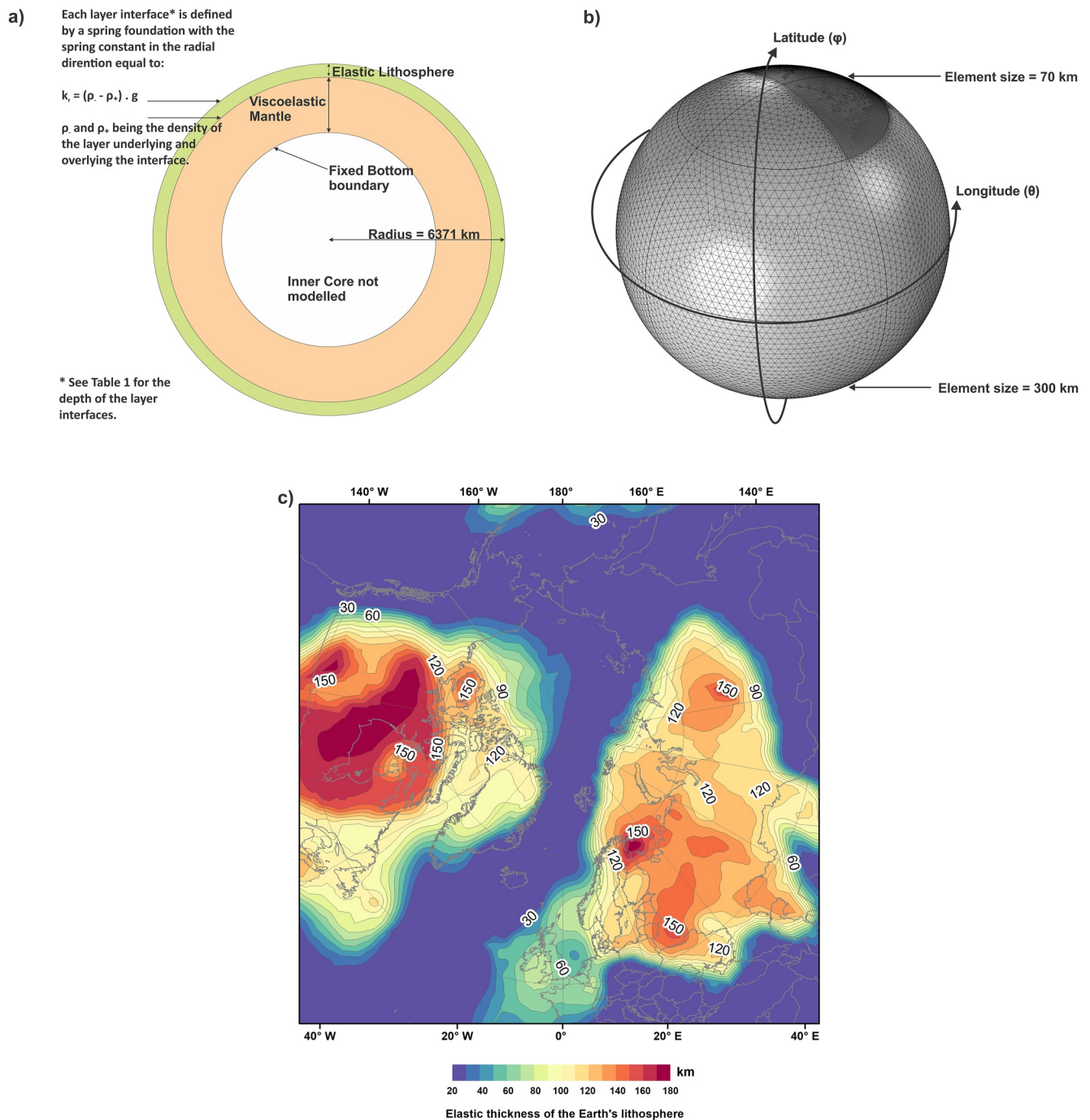


**Figure 2.** (a) Model set-up and (b) mesh structure for the viscoelastic spherical Earth model used in this study. (c) Map of the elastic thickness of the Earth's lithosphere, based on Tesauro et al (2013; personal communication), used in model VL20-175.

rebound of the lithosphere over an area that laterally extends to about 1,800 km in the N-S dimension and 1,200 km in the E-W dimension. The center of the rebound is in the western part of the Bay of Bothnia where the maximum uplift rate reaches 9.6 mm/yr. From that point, the vertical velocity decreases radially. In the peripheral bulge, the crust is currently actively subsiding at a rate of 1.40 mm/yr over the north of the Netherlands. The average of the uncertainties over the processed vertical velocities is about 0.23 mm/yr.

Comparing model prediction with observational data in Svalbard is more difficult because of the limited number of GPS stations over the archipelago. In Auriac et al. (2016) the authors show the present uplift over Svalbard

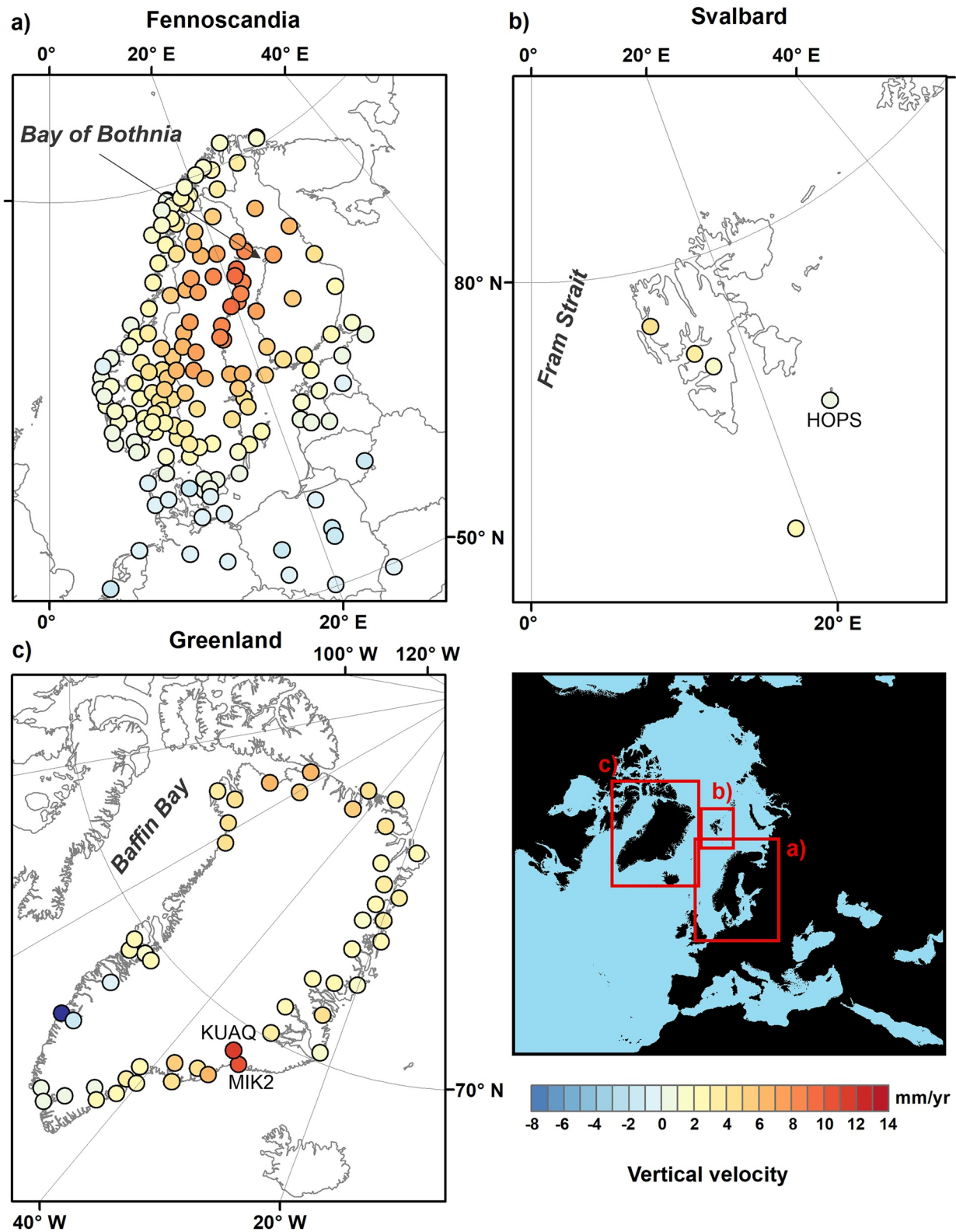


**Figure 3.** Map of present-day vertical velocity measured by GPS within the ITRF2008 reference frame and from: (a), BIFROST2015 (Auriac et al., 2016; Kierulf et al., 2021) (b), Svalbard (Auriac et al., 2016, Kierulf personal communication) and (c) the Greenland network—GNET (Khan et al., 2016).



(see Figure 3b). We observe that the minimum uplift is in the Hopen Island (station HOPS) and the maximum in the northwest of Svalbard (station NYAL) with values equal to 1.0 and 4.9 mm/yr, respectively. Note that station HOPS is largely unstable and thus data from this location are considered unreliable (Auriac et al., 2016). The average uncertainty of the processed vertical velocities is about 0.02 mm/yr, which is clearly underestimated (Auriac et al., 2016; King et al., 2010).

The Greenland GPS network (GNET) only covers the edge of the island, the only part of land that is not ice covered (see Figure 3c). The data set that we use for this study is processed using the ITRF2008 reference frame and shows that the edge of the island is currently rebounding at a rate that average 3.5 mm/yr (Khan et al., 2016). The MIK2 and KUAQ stations next to the Gunnbjorn region show higher vertical velocities than in the rest of the island where the uplift rate exceeds 10 mm/yr. The authors explain that this local variation is due to the presence of a temperature anomaly in the mantle underlying this region, induced by the migration of the Icelandic hotspot (Jakovlev et al., 2012; Rogozhina et al., 2016). The average of uncertainties of the processed vertical velocities is about 0.43 mm/yr.

We estimate the performance of each of our Earth models by calculating the misfit  $\chi^2$  between the predicted vertical velocities with the GPS data presented above:

$$\chi^2 = \frac{\sum \left( \frac{v_{obs} - v_{model}}{\sigma_{obs}} \right)^2}{N} \quad (3)$$

Where  $v_{obs}$  and  $v_{model}$  are the vertical velocities obtained from GPS measurement and predicted by the model respectively,  $N$  the number of GPS stations and  $\sigma_{obs}$  the uncertainties of the observed vertical velocities. For each model, the lowest  $\chi^2$  value indicates the best-fit model. Note that we exclude the HOPS, MIK2 and KUAQ stations in the calculation of the  $\chi^2$  as they are either considered unreliable or describe an uplift signal that cannot be explained by GIA. For the remaining four GPS stations in Svalbard, we use a constant  $\sigma_{obs}$  of 0.3 mm/yr (Kierulf, personal communication) instead of the underestimated uncertainties presented in Auriac et al. (2016).

### 3. Results

#### 3.1. Present Day Vertical Velocities Predicted by the Numerical Models and Comparison With GPS Constraints

In Figures 4 and 5, we show how our Earth models respond to deglaciation by presenting maps of vertical displacement rates at present time over Northern Europe, Svalbard and Greenland. We first note that the overall pattern of vertical velocities in the three GIA models is similar. It can be described by: (a) a positive vertical velocity (i.e., uplift) in the subsidence bowls centered on formerly glaciated regions (e.g., Fennoscandia, Barents Sea), (b) a negative vertical velocity (i.e., subsidence) in the forebulge surrounding the edge of the former ice-sheets, and (c) a negative vertical velocity in subsiding ice-covered regions (e.g., center Greenland). However, each GIA model exhibits significant variation in the magnitude and spatial extent of the glacial rebound.

Model TE60 has overall the fastest present uplift rate over Fennoscandia (see Figure 4) with a maximum uplift velocity of 11 mm/yr along the northern shore boarding the Bay of Bothnia. In Svalbard, model TE60 and VL20-175 exhibit uplift rates of a similar magnitude, exceeding 6 mm/yr in the east of the archipelago. In the forebulge surrounding the former Eurasian ice sheet, the subsidence rate exceeds 3 mm/yr in the Atlantic Ocean, around the 10°E meridian and 73°N parallel, in all three models. When comparing our predicted uplift rates with GPS observations over Fennoscandia (Figures 6a–6c), we see that the misfit between the measured and predicted uplift is equal to 163 for model TE60, 145 for model TE120 and 136 for model VL20-175. We find the largest misfits in the south of Norway, around the Oslo rift, where the uplift difference exceeds 2.5 mm/yr for all three Earth models. The best fit between observed and predicted solutions is given around the Bay of Bothnia, where the present-day uplift rate is the fastest within the modeled region (Figures 6a–6c). However, the location of the uplift center observed from GPS data is located more to the south, by about 300 km, than solutions predicted by our models. In Svalbard, we note that the misfit between the predicted and observed uplift along the four GPS stations is 149 for model TE60, 165 for model TE120 and 138 for model VL20-175 (Figures 6g–6i). The vertical velocities predicted by our model are overall too slow in comparison to GPS data.

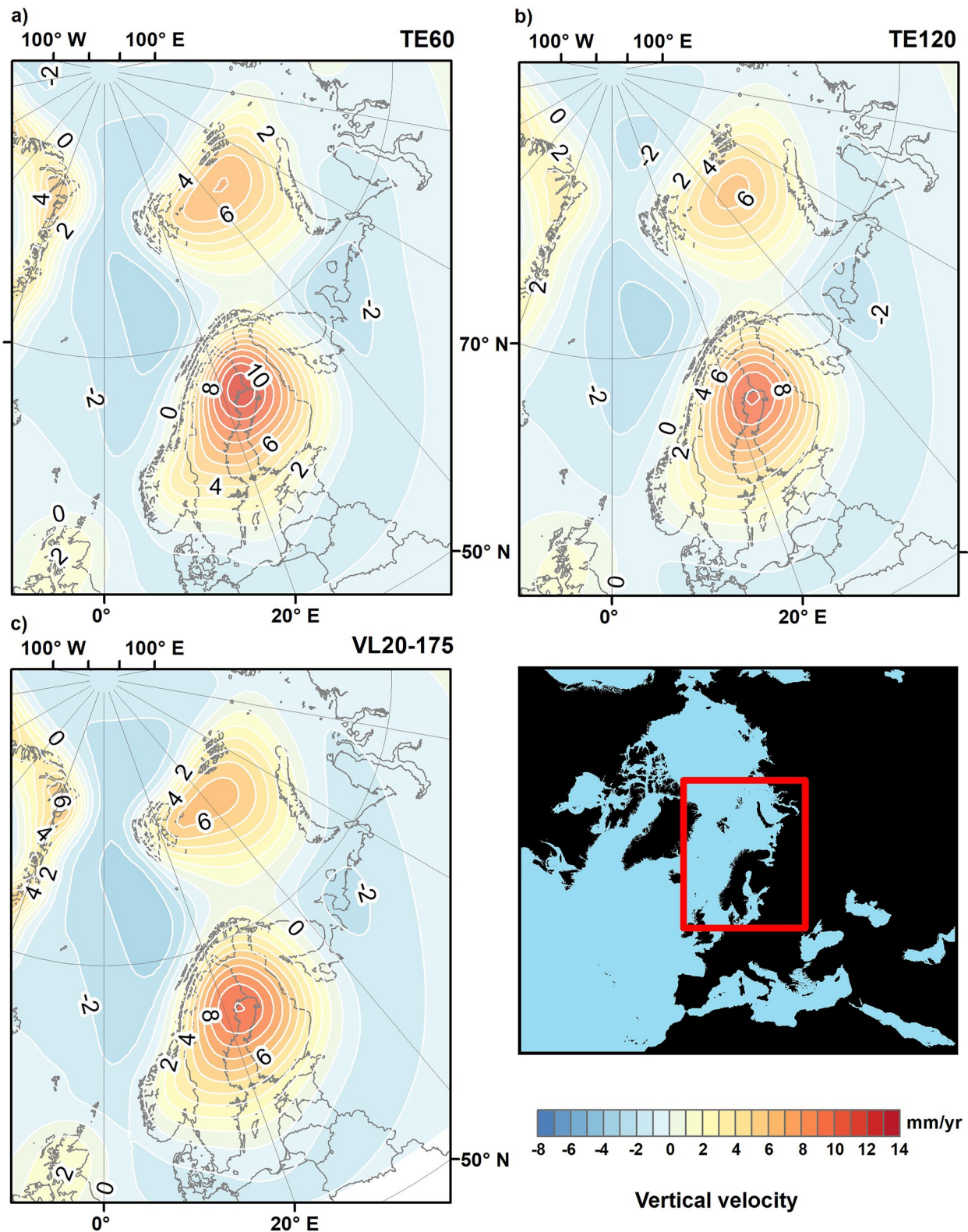


**Figure 4.** Present-day map of the vertical velocity magnitude computed for our three Earth models, TE60, TE120 and VL20-175 over Fennoscandia, Svalbard and the Barents Sea, using our composite ice model.

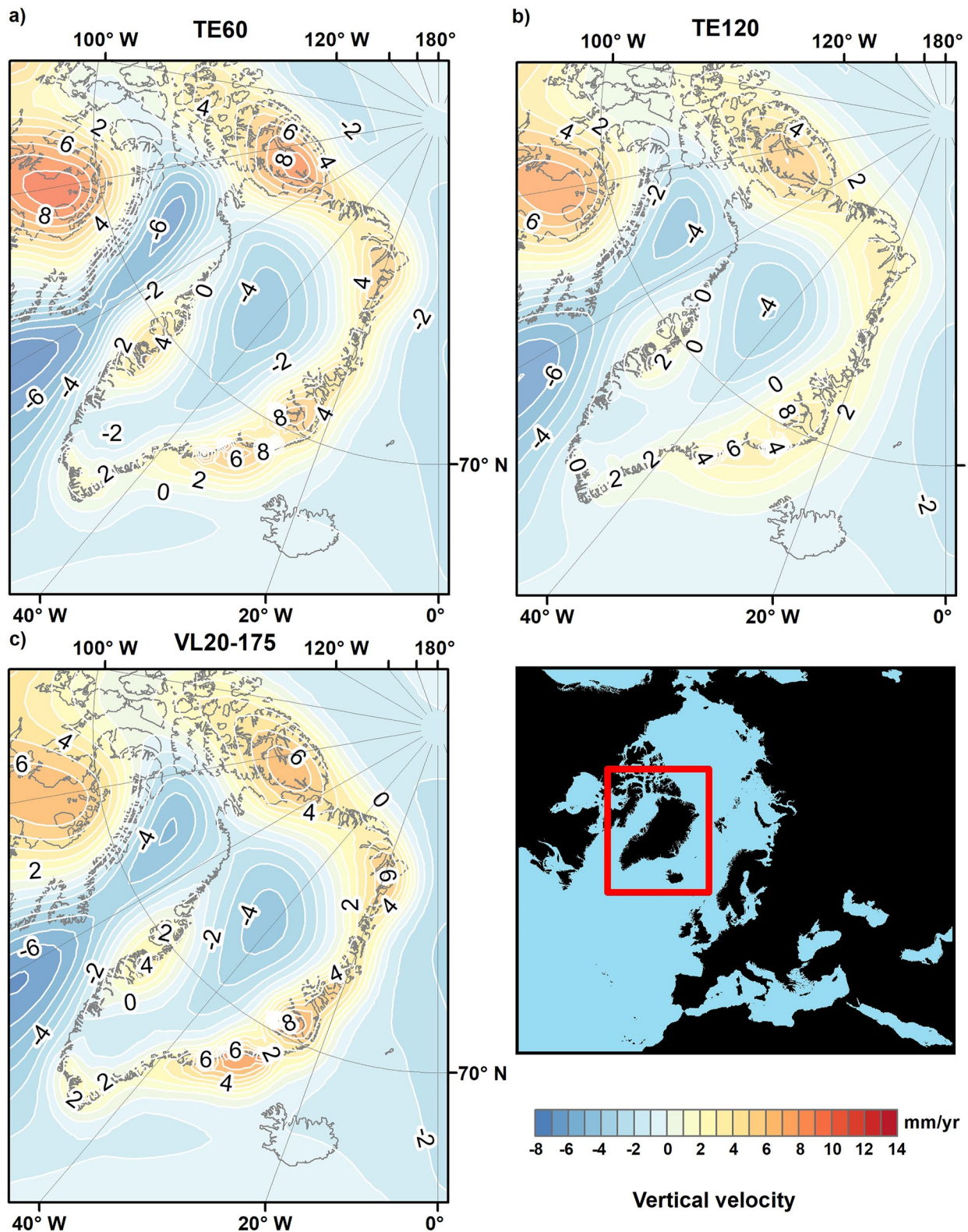


**Figure 5.** Present-day map of the vertical velocity magnitude computed by our three Earth models, TE60, TE120 and VL20-175 over Greenland, using our composite ice model.

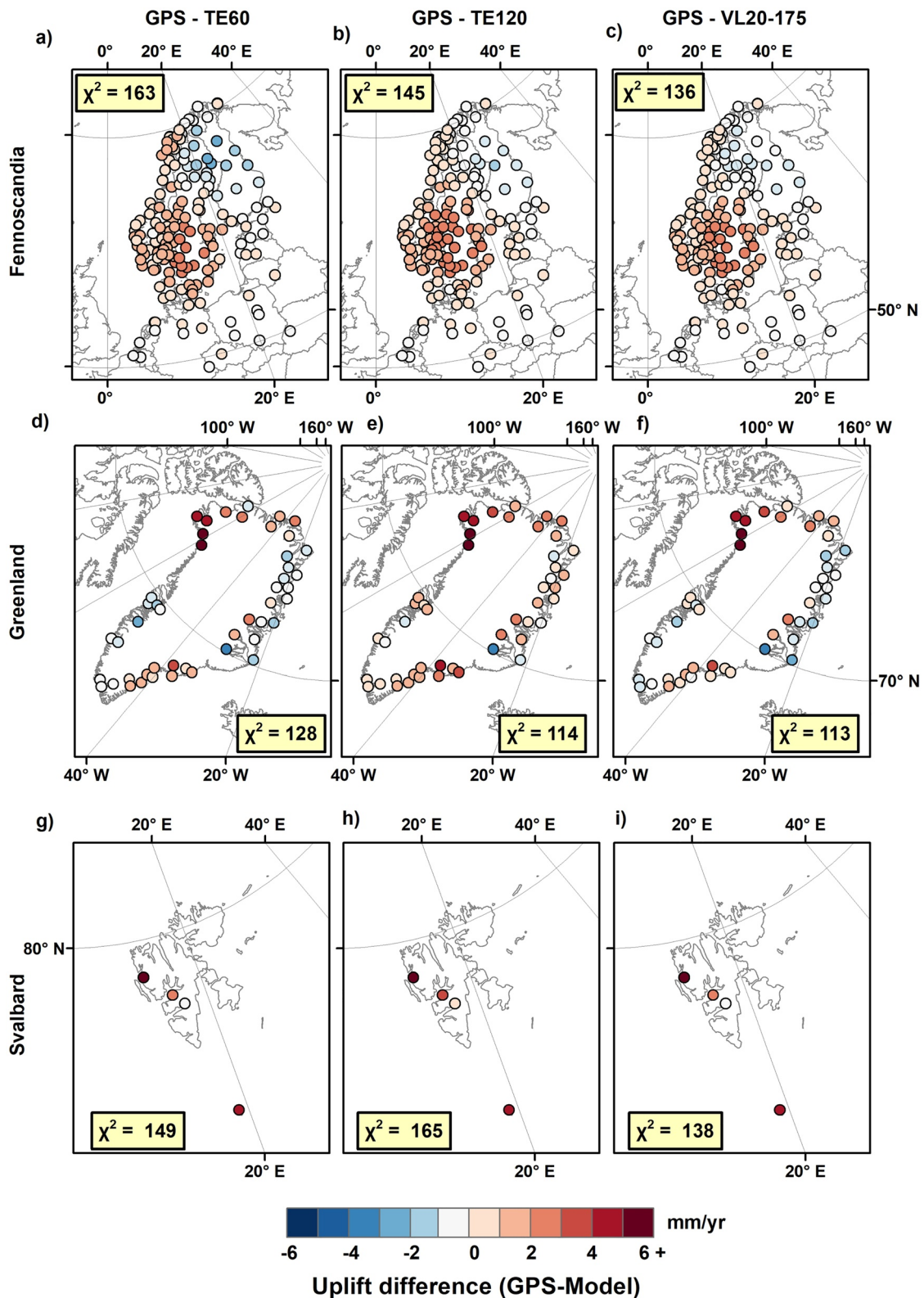


**Figure 6.** Map of the present-day differences between GPS uplift data and predicted solution from our three Earth models. The difference and  $\chi^2$  are computed over (a–c) Fennoscandia, (d–f) Greenland and (g–i) Svalbard.

In Greenland the models predict a more complex pattern of the vertical velocity field than in Fennoscandia and Svalbard (Figure 5). For our three GIA models, the center of Greenland is currently subsiding at a rate that exceeds 4 mm/yr. The edge of the island, however, is currently rebounding due to the retreat of the Greenland ice sheet. All three models show vertical velocities that exceed 6 mm/yr in the southeast and north coast of Greenland. In the forebulge areas, the subsidence rate is higher than 4 mm/yr in the north and south of Baffin Bay. When comparing our predicted vertical velocity field with GPS observations, we show that solutions predicted by our three models are in good agreement (Figure 6). There is significant mismatch along the northwest coast (Figures 6d–6f), where our model predicts subsidence ( $\sim 1\text{--}2$  mm/yr) at present time while GPS data indicates an uplift ( $\sim 3\text{--}4$  mm/yr). The discrepancy is likely due to the Huy3 ice reconstruction not accounting for the Inuitian ice sheet, which would produce a thicker ice cover in the north and northwest of Greenland (Lecavalier et al., 2014). That additional weight of the ice would lead to additional subsidence at LGM, and thus greater rebound during the Holocene deglaciation. The best-fit  $\chi^2$  in Greenland is given by model VL20-175 with a value equal to 113, compared to 128 and 114 for model TE60 and TE120, respectively (Figures 6d–6f).

Overall, model VL20-175 gives the best fit compared to the geodetic constraints. We thus decided to present the glacial stresses from this specific Earth model in the following sections and discuss how the results of TE60 and TE120 differ from that.

### 3.2. Evolution of the Glacially Induced Stress and Vertical Surface Displacements From 122.8 kyrs BP to Present—Model VL20-175

In this section, we present the stress and displacement fields induced by the advance and retreat of continental ice sheets on our earth model VL20-175. We first present the stress and displacement fields as maps and vertical cross sections of the maximum horizontal stress  $\sigma_H$  and maximum shear stress  $\tau_{\max}$ , plotted at two separate times: (a) 23 kyrs BP when the Eurasian ice sheet is at its most recent maximum extent (LGM), and (b) at present when the ice sheet has vanished in Northern Europe. The maximum horizontal stress,  $\sigma_H$ , describes the most compressive stress in the horizontal plane. It is generally an interesting component to analyze in the context of geological system interactions because it shows stress in the same plane than major geological structures (e.g., plate boundary, faults, mountain belt etc.) and makes it easier to compare with tectonic stresses also often plotted in the horizontal plane. The maximum shear stress  $\tau_{\max}$  describes half the difference between the maximum and the minimum principal stresses and is closely related to the ability of the material to slip along a preferential plane. In addition, we show the temporal evolution of the maximum horizontal and shear stresses, together with the vertical stress, at key locations, from 122.8 kyrs BP to present.

#### 3.2.1. Glacial Stresses and Vertical Surface Displacement at LGM (T = 23 kyrs BP)

In Figure 7a, we present the glacially induced vertical surface displacement ( $U_z$ ) over Northern Europe for model VL20-175 at the LGM. Two subsidence bowls form under the weight of the ice. The northernmost, centered on the northern Barents Sea, reaches a maximum subsidence of 400 m, with horizontal dimensions of 1,900 km in the E-W direction and 1,600 km in the N-S direction (Figure 7a). The southern bowl, centered on Northern Scandinavia, reaches a maximum subsidence of 450 m, with horizontal dimensions of 2,300 km in the E-W direction and 2,200 km in the N-S direction (Figure 7a). Looking at the glacially induced stress field, we note that  $\sigma_H$  is compressive in glaciated regions, and oriented approximately perpendicular to the long axis of the ice sheet (Figure 7d). We find the  $\sigma_H$  maxima (with magnitudes as high as 24–28 MPa) located 130 km West and 120 km north of the Barents Sea and Fennoscandian bowl centers, respectively. Along the peripheral bulge (10–20 m high on average) and upper flank of the bowl,  $\sigma_H$  is tensile, with magnitude as low as  $-6$  to  $-8$  MPa, and generally oriented parallel to the edge of the ice sheet (Figure 7d). The maximum shear stress ( $\tau_{\max}$  in Figure 7g) is localized in the southern Barents Sea ( $\tau_{\max} = 6\text{--}7$  MPa) collocated with the tensile bands that forms along the ice sheet borders ( $\tau_{\max} = 4\text{--}6$  MPa). In northernmost Sweden and east of Svalbard  $\tau_{\max}$  exceeds 4 MPa (Figure 7g).

Over Greenland, the pattern of  $\sigma_H$  and vertical surface displacement is essentially similar to that in Northern Europe (Figures 7b and 7e). We find that the wavelength of the Greenland depression bowl is about 2,200 km long in the E-W direction and 3,100 km long in the N-S direction. The magnitude of the subsidence at the bowl's center reaches a maximum of 650 m (Figure 7b). The thicker Greenland ice cover leads to  $\sigma_H$  being overall higher than in Northern Europe, with values exceeding 40 MPa at the center of the island. Along the upper flank of the bowl and forebulge (about maximum 30–60 m in height), tensile  $\sigma_H$  can locally be lower than  $-10$  MPa, as in the

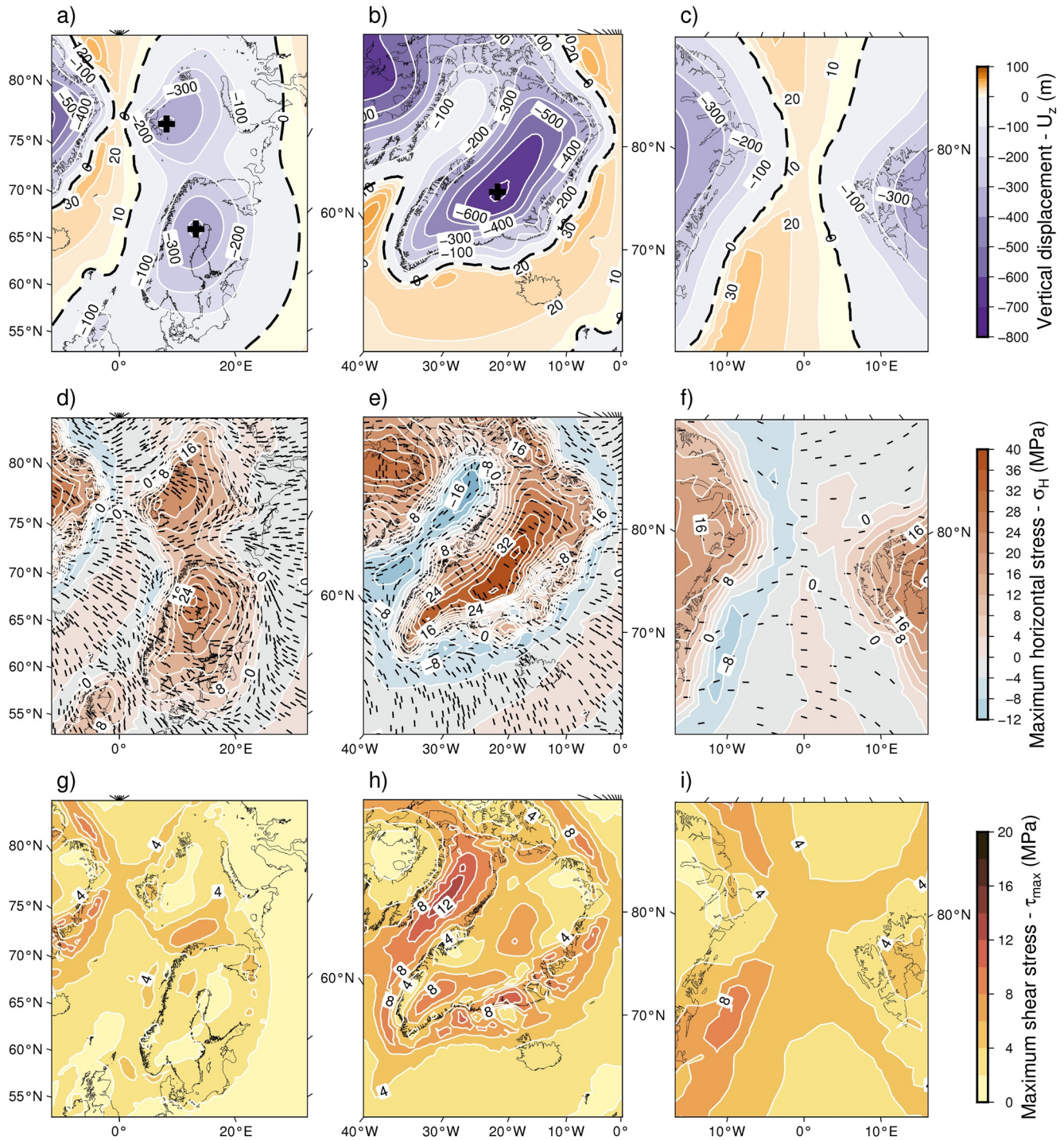


**Figure 7.** Maps of (a–c) the vertical displacement at surface level, (d–f) the maximum horizontal stress and (g–i) the maximum shear stress computed for model VL20-175 at 2.5 km depth and at the LGM (23 kyrs BP), over (a, d, g) Fennoscandia, (b, e, h) Greenland and (c, f, i) the Fram Strait. The dashed lines and black crosses define the 0 m contour and center of the subsidence bowls, respectively.

Greenland Sea and in the north of Baffin Bay and is overall oriented parallel to the ice sheet boundary. Maximum shear stresses can be as high as 12–13 MPa in the north of Baffin Bay (Figure 7h). Between thick ice regions along the east coast of Greenland, depression zones are characterized by  $\tau_{max}$  as high as 8–9 MPa (Figure 7h). In the subsidence bowl formed in Greenland, we note that the maximum shear stress exceeds 8 MPa in the south and at the center of the island (Figure 7h).

The Fram Strait region sits at the junction of the forebulges formed at the periphery of the Greenland and Eurasian ice sheets (Figure 7c). The magnitude of  $\sigma_H$  reaches a minimum of  $-8$  MPa close to the east coast of Greenland, and range between 4 and  $-2$  MPa off the west Svalbard coast (Figure 7f). In between the two regions,  $\sigma_H$  is overall oriented E-W and thus perpendicular to the edge of the Greenland and Eurasian ice sheets. We note a N-S oriented, ca. 150 km wide band of compressive  $\sigma_H$  in the middle of the Fram-Strait, at a latitude of  $80^\circ$ , where  $\sigma_H$  varies between 0 and 4 MPa (Figure 7f). The areas of high shear stress follow that of the tensile stresses (i.e., maximum  $\tau_{\max}$  are found along the flanks of the forebulge between Greenland and Svalbard) where stresses are associated with the forebulge. The maximum shear stress increases westwards across the Fram Strait from 2 MPa close to Svalbard, to 4–8 MPa close to Greenland (Figure 7i).

When comparing our earth models at the LGM over Fennoscandia (Figure B1), Greenland (Figure B2) and the Fram Strait (Figure B3), we found that TE120 predicts GIA stress magnitude that are 10%–20% higher than for TE60. Generally, we find that VL20-175 features similar  $\sigma_H$  and  $\tau_{\max}$  field as for TE120 over Fennoscandia (Figures B1d, B1f, B1g, and B1i), where the elastic thickness of the Earth's lithosphere is about 100–120 km thick in VL20-175. Whereas over Svalbard, the Barents Sea and Greenland,  $\sigma_H$  and  $\tau_{\max}$  fields predicted by model VL20-175 are closer to solutions from model TE60 (Figures B1e, B1f, B1h, and B1i, and B3e, B3f, B3h, and B3i). Looking at the general orientation of  $\sigma_H$  between each Earth model (Figures B1d, B1e and B1f, B2d, B2e, and B2f, and B3d, B3e and B3f), we first note that the global pattern follows the same behavior irrespective of the Earth model used, with  $\sigma_H$  oriented parallel to the edge of the ice sheet and perpendicular to the long axis of the ice sheet in the interior of glaciated areas. However, the direction of  $\sigma_H$  in the Fram Strait does not follow that trend in model VL20-175 (see Figure 7f) where  $\sigma_H$  is oriented E-W (i.e., perpendicular to the ice-sheet margins).

Looking at Figure B3a, which displays the vertical surface displacement  $U_z$  for our TE120 model, we can see that the subsidence bowls around the Barents Sea and Greenland connects at the LGM in the Fram Strait. As the Fram Strait is located along the edge of the subsidence bowls, which are oriented N-S, the direction of  $\sigma_H$  also follows a N-S orientation (Figure B3d). In the TE60 model the Greenland and Barents Sea bowls barely touch (Figure B3b) while in VL20-175 the same subsidence bowls are separated by about 150–200 km at the closest distance (Figure B3c). As the Fram Strait is located outside the Greenland and Barents Sea bowls in model VL20-175, the orientation of the  $\sigma_H$  stress is roughly perpendicular to their edges, thus E-W (Figure B3f). Our model TE60 is a boundary case where Fram Strait is located more or less along the edges of the Greenland and Barents Sea bowls which in combination results in the N-S orientation of  $\sigma_H$  (Figure B3e).

Overall,  $\tau_{\max}$  localize at similar location in all three models (Figures B1g, B1h, and B1i, B2g, B2h, and B2i, and B3g, B3h, and B3i), that is, along the tensile region that surrounds the glaciated lands and where the ice sheet forms a depression (steep gradient of the ice thickness). Like the  $\sigma_H$  field, we note larger spatial variation in the  $\tau_{\max}$  distribution for model TE60 and VL20-175, where the elastic thickness of the Earth's lithosphere is in part thinner than in model TE120.

### 3.2.2. Glacial Stresses and Vertical Surface Displacement at Present Time

In Figure 8d, we show the present-day maximum horizontal stress component at 2.5 km depth induced by glacial rebound over Northern Europe for model VL20-175. We find that the present day  $\sigma_H$  has decreased by a factor of 3–4 since the LGM but the peaks of maximum horizontal stress are observed at the same locations (8–9 MPa in the Barents Sea and 4 MPa in the Bay of Bothnia) as during the LGM. Moreover, we observe significant changes in the orientation of  $\sigma_H$  between the LGM and present, especially in Fennoscandia where the ice completely vanished at 9.7 kyrs BP (Figure 8d). The maximum horizontal stress direction generally follows a circular pattern centered on the rebounding depression bowls that are in the Barents Sea and Fennoscandia (Figure 8a). Along the edge of the former ice sheet,  $\sigma_H$  stresses stay negative but are tending to 0 MPa (Figure 8d) because of the collapse of the peripheral forebulge. The high  $\tau_{\max}$  zone that was concentrated in the southern Barents Sea at the LGM has now almost vanished (Figure 8g). Over Northern Europe,  $\tau_{\max}$  has overall decreased since the end of glaciation of the Eurasian ice sheet. However, patches of high  $\tau_{\max}$  remain in northern Sweden and over Svalbard and its west margin, where  $\tau_{\max}$  exceeds 2–3 MPa (Figures 8g and 8i).

At present, the Greenland ice sheet has partially melted since the 16.5 kyrs BP glacial maximum, but about 55%–60% of the ice volume remains. First, we note that the retreat of the ice body toward the inland induces rebound of the coastal area (Figures 5b and 5c). Meanwhile, an overall thickening of the ice sheet at the center of the island, between 23 and 16.5 kyrs, has induced further subsidence by about 40 m. The combined effect of

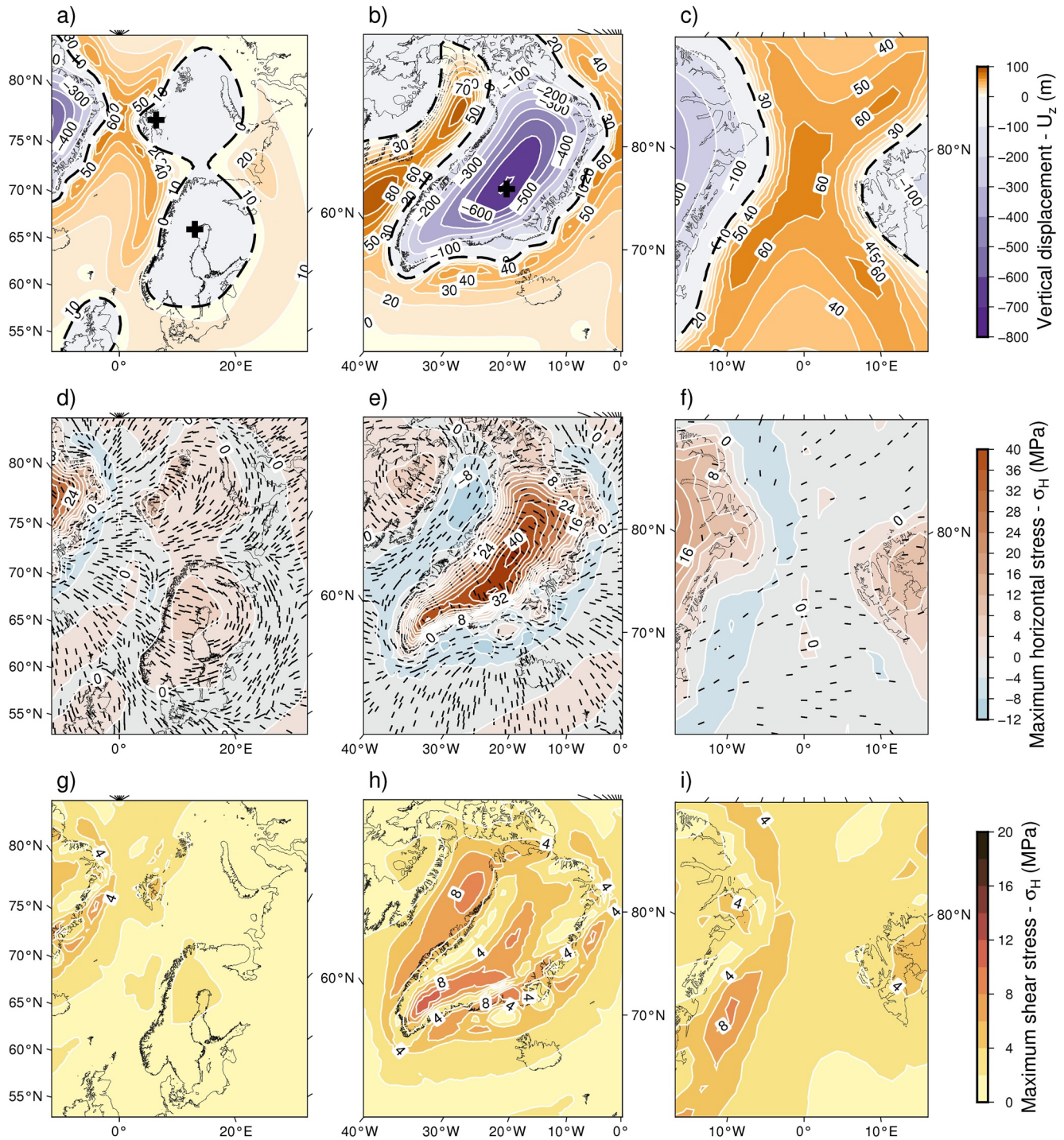


**Figure 8.** Present-day maps of (a–c) the vertical surface displacement, (d–f) the maximum horizontal stress and (g–i) the maximum shear stress computed for model VL20-175 at 2.5 km depth, over (a, d, g) Fennoscandia, (b, e, h) Greenland and (c, f, i) the Fram Strait. The dashed lines and black crosses define the 0 m contour and center of the subsidence bowls, respectively.

the rebounding coast around Greenland together with the further subsidence of the center produces a smaller but deeper bowl than at the LGM (Figures 7 and 8b). This results in a steeper bowl flank close to its center and thus larger maximum horizontal stress (i.e., 47 MPa at that location; Figure 8e). We do not find any major changes in the orientation pattern of  $\sigma_H$  between 23 kys BP and present time, except in the east of Greenland where the azimuth of  $\sigma_H$  is rotated by about 90° (Figure 8e). Around the periphery of Greenland, we observe a 10%–30%



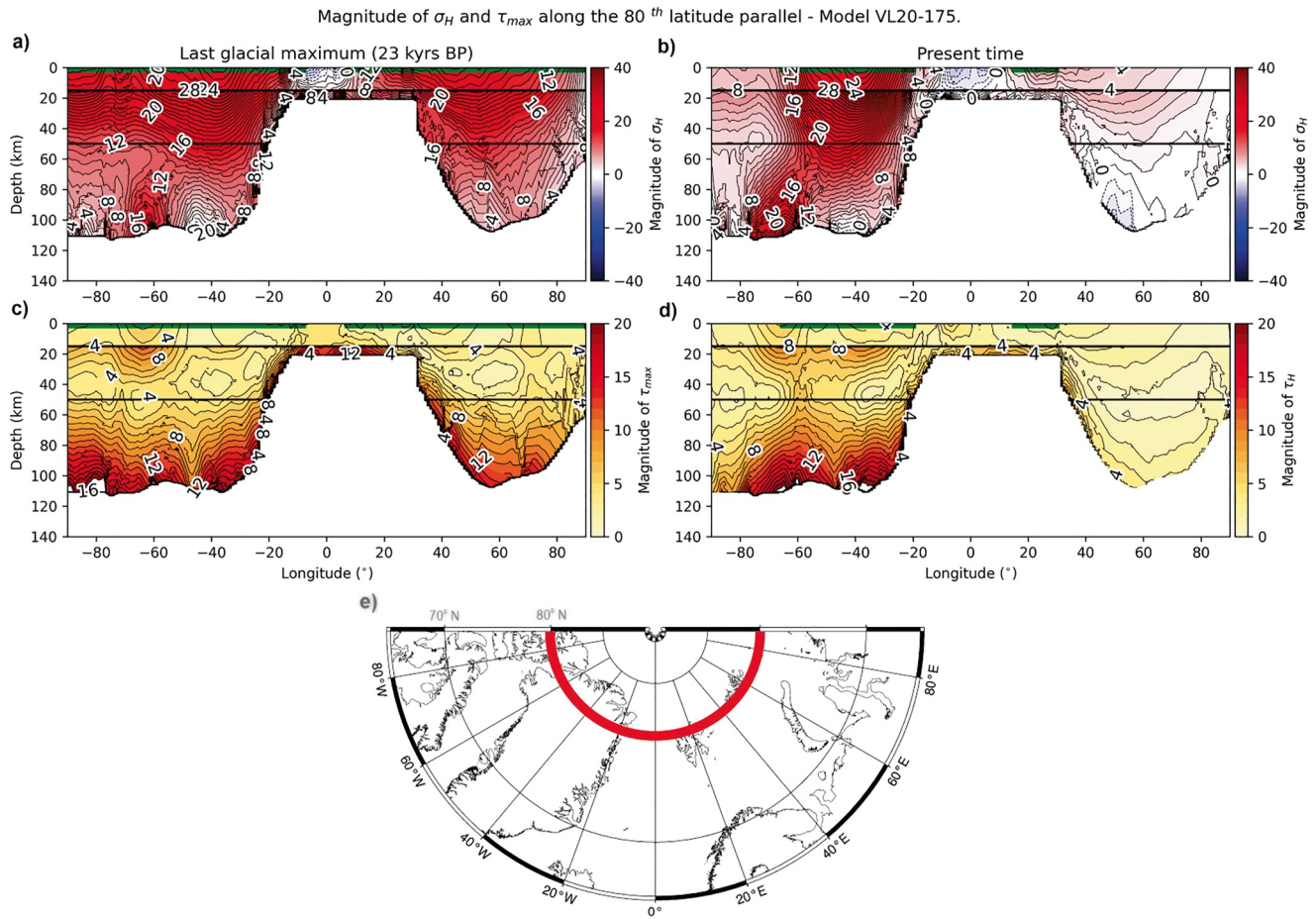


**Figure 9.** Vertical cross-section of the (a, c) maximum horizontal stress and (b, d) maximum shear stress along the 80th latitude parallel (between longitude  $-90^\circ$  and  $90^\circ$ ), at (a, b) the LGM (23 kyrs BP) and (c, d) present time. Green horizontal lines at the surface show the extent of the ice sheets. (e) map of the Arctic between longitude  $-90^\circ$  and  $90^\circ$ , the red line shows the location of the cross section.

reduction of the  $\tau_{\max}$  magnitude since LGM (Figure 8h), mostly induced by the retreat and melting of the Greenland and North American ice sheets. Patches of high  $\tau_{\max}$  remains in the Baffin Bay ( $\tau_{\max} = 8$  MPa) and in remaining glaciated areas like central and south Greenland ( $\tau_{\max} = 8\text{--}11$  MPa).

The Fram Strait region is still affected by tensile horizontal stresses at 2.5 km depth at present time (Figure 8f). The magnitude of  $\sigma_H$  is however closer to 0 MPa (less tensile) than at LGM, with a local minimum off the east coast of Greenland that changes between the LGM and present day from  $-10$  MPa to  $-8$  MPa (Figure 8f). In this region, we note that the direction of  $\sigma_H$  stays overall perpendicular to the former Eurasian ice sheet off the west coast of Svalbard. In the eastern Fram Strait, we observe a migration of the 0 MPa isoline toward Svalbard because of the melting of the Eurasian ice sheet. The maximum shear stress in the west Svalbard margin has decreased by 10%–20% since the LGM (Figure 8i).

When comparing stresses from the three Earth models over formerly glaciated regions, we notice that GIA induced stresses in model TE120 (Figures C1d and C1g) are about 30%–50% lower than in model TE60 at present day (Figures C1e and C1h). This implies a faster decay of the GIA induced stresses since the beginning of deglaciation for model TE120 (Figures B1d, B1g, C1d, and C1g). Overall, the differences between each Earth models that we noted for the LGM still hold at present time.

### 3.2.3. Stress Depths Sections at LGM (T = 23 kyrs BP) and Present Time

In Figure 9, we present depth profiles down to 140 km along the northern 80th parallel, which crosses the Arctic region from Northern Canada to the Severnaya Zemlya archipelago. As for the maps of Sections 3.2.1

and 3.2.2, we present the maximum horizontal stress and maximum shear stress magnitude at the LGM and present time.

As inferred from the stress maps,  $\sigma_H$  at LGM (see Figure 9a) is in compression below the ice sheet and in tension under the forebulge. At near surface level,  $\tau_{\max}$  focus (Figure 9b) under the center of the Greenland ice sheet ( $\tau_{\max} > 6$  MPa) and in the Fram Strait ( $\tau_{\max} > 5$  MPa). Across the 15 km border, we note an increase of the  $\tau_{\max}$  that correspond to the stepwise increase of Young's modulus set up in the model, which of course is a model simplification. Overall,  $\tau_{\max}$  peaks at the contact between the elastic lithosphere and viscoelastic mantle, where the magnitude exceeds 16 MPa (Figures 9b and 9c).

At present day (see Figure 9c),  $\sigma_H$  follows the general distribution described at the LGM over Northern Europe, but its magnitude has decreased by a factor 3–4, as shown on the stress maps (Section 3.2.2). Because of the ice-sheet disappearance, the peripheral bulge collapses and spreads laterally, so that the bend where  $\sigma_H$  is tensile is less steep but spreads laterally as well. We note a similar distribution of  $\tau_{\max}$  in Greenland at present time as during the LGM (see Figure 9d). Whereas in North America, Svalbard and the Barents Sea, the retreat and melting of the ice sheets leads to a reduction of  $\tau_{\max}$  by a factor 2–4. This observation applies at near surface level and at depth.

### 3.2.4. Temporal Evolution of the Glacial Stress Field

Figure 10 shows the evolution in time of the magnitude and direction of the maximum horizontal stress ( $\sigma_H$ ), the magnitude of the minimum horizontal stress ( $\sigma_h$ ), maximum shear stress ( $\tau_{\max}$ ) and vertical stress ( $\sigma_v$ ). Each of the stress components are calculated at 2.5 km depth in model VL20-175, at locations along the north coast of the Bay of Bothnia, the Barents Sea, the west-Svalbard margin, and central Greenland. In Figure 10,  $\sigma_v$  is reflecting the ice load and can be used as a proxy for the thickness of the ice through time.

Three major glacial advances are recorded over Northern Europe during the last glacial cycle, separated by approximately 12 and 20 kyrs of ice-free conditions (Figures 10a and 10b).  $\sigma_H$  and  $\sigma_h$  first follows the build-up of the ice and then  $\sigma_H$  continues to grow to surpass  $\sigma_v$ , as the lithosphere flexes and the mantle is slowly displaced. During the last glacial phase, we note that  $\sigma_H$  peaks at 24 MPa in the Barents Sea and 29 MPa over Northern Sweden (see Figures 10a and 10b). At times of ice-free conditions, the horizontal stresses slowly decrease due to post-glacial rebound, at a rate that depends on the mantle viscosity. We do not notice any major change through time in the azimuth of  $\sigma_H$  over the Barents Sea, which overall stays oriented N-S (direction of  $0^\circ$ ). In Northern Sweden, the direction of  $\sigma_H$  fluctuates between  $20^\circ$  during the first glacial buildup, and  $-45^\circ$  at present time. Focusing on the maximum shear stress in the Barents Sea and Northern Sweden, we find that  $\tau_{\max}$  peaks during the 82, 56 and 15–10 kyrs BP deglaciations of the Eurasian ice sheet, with magnitudes as high as 4–8 MPa.

In the west-Svalbard margin (Figure 10c),  $\sigma_H$  changes between a compressive ( $\sigma_H$  is equal to 0.5 MPa at  $t = 100$  kyrs BP) and tensile regime over time ( $\sigma_H$  is equal to  $-1.5$  MPa at  $t = 65$  kyrs BP and 0 MPa at  $t = 30$  kyrs). At present,  $\sigma_H$  remains tensile ( $\sigma_H = -2.2$  MPa) in the area and is oriented E-W (direction of about  $-85^\circ$ ). Between 122.8 kyrs BP and present,  $\sigma_h$  stays tensile and reaches a minimum of about  $-10$  MPa during the deglaciation of the Barents Sea ice sheet at 82, 56 and 15 kyrs BP. Looking at the evolution of  $\tau_{\max}$  in the Fram Strait, we note that  $\tau_{\max}$  follows the same behavior than in the neighboring regions of the Barents Sea and Fennoscandia (Figures 10a–10c) and reaches a maximum magnitude of 4–5 MPa at 82, 56, and 15 kyrs BP.

In central Greenland, the thickness of the ice sheet does not evolve much in time (see Figure 10d). We note a gradual buildup of  $\sigma_H$  and  $\sigma_h$  during the initial glaciation phase. From 80 to 12 kyrs BP,  $\sigma_H$  is more or less constant, at about 43 MPa, which indicates that flexure of the lithosphere changes little at this site after the first 40 kyrs. At later times, there is an increase in  $\sigma_H$  to 47 MPa that correlates with the retreat of the ice toward the inland and an overall thickening of the Greenland ice sheet between 23 kyrs and present (see Section 3.2.2). In central Greenland, the evolution in time of  $\tau_{\max}$  is similar to  $\sigma_H$  and peaks at present time with a maximum value of 8.5 MPa.

### 3.3. Implication of GIA Stresses for Arctic Faulting and Associated Methane Seepage

We have seen in the preceding sections that an ice sheet induces significant time-varying vertical and horizontal stresses in the Earth's crust. The glacial stresses interact with the pre-existing in-situ stress field and potentially

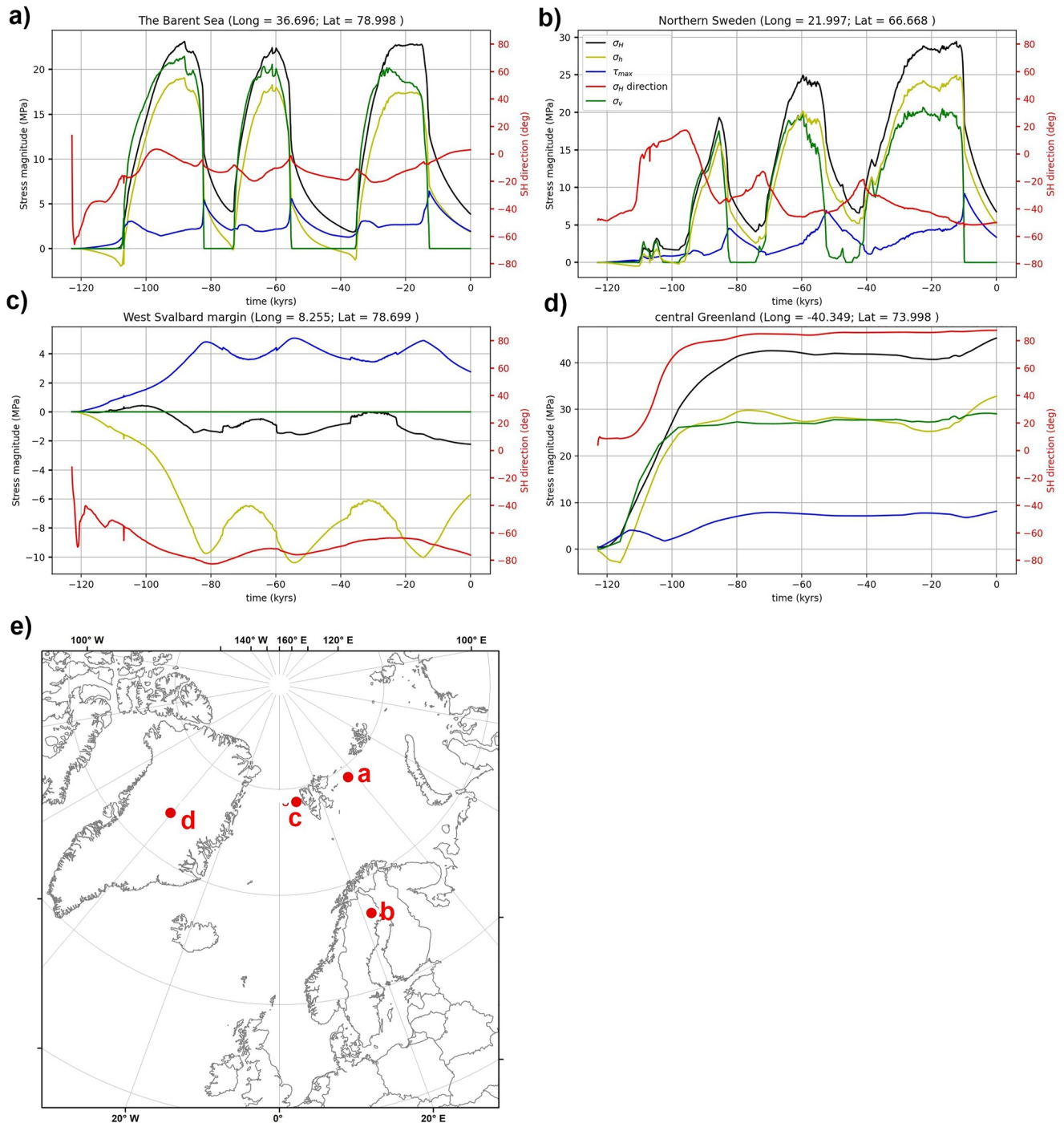


**Figure 10.** Temporal evolution of  $\sigma_v$ , the vertical stress magnitude (green curve),  $\tau_{max}$  maximum shear stress (blue curve),  $\sigma_h$  the minimum horizontal stress magnitude (yellow curve),  $\sigma_H$  the maximum horizontal stress magnitude (black curve) and direction (red curve). Four sites are selected: (a) The North of the Barents Sea, (b) Northern Sweden, (c) The passive margin of West Svalbard and (d) the center of Greenland. The locations of each site are projected on a map of Greenland and Fennoscandia (e).

has important implications for the evolution of neo-tectonic phenomena and associated processes along continental margins (e.g., Lund et al., 2009; Wu et al., 1999). Moreover, various studies indicate that glacially induced stresses can trigger large magnitude earthquakes, as indicated by fault scarps in Northern Europe (Lagerbäck et al., 2008 and reference therein; Steffen et al., 2021). For example, the Pärvie fault in the Lapland province has a  $\sim 15$  m high fault scarp (Lagerbäck, 1992), inferred to have formed about 9,000 years ago during a  $\sim M_w = 8.0$

earthquake (Lindblom et al., 2015). Further GIA modeling investigations of glacial stresses and their effect on fault stability have shown that earthquake frequency in glaciated regions is influenced by the evolution in time of the ice sheets (e.g., Hampel & Hetzel, 2006; Olivieri & Spada, 2015; Steffen et al., 2014). These studies overall agree on that glacial loading is generally associated with a seismically quiet period in the ice-covered region, whereas seismicity could be promoted by glacial unloading and lithospheric rebound. Calculating glacial stresses is therefore critical for understanding fault behavior in formerly glaciated areas like Fennoscandia (Lund et al., 2009; Steffen et al., 2014; Wu et al., 1999) or in Greenland where the ice sheet is rapidly melting (Olivieri & Spada, 2015; Steffen et al., 2020).

The glacial stress models suggest that there are regions where glacial stresses have been persistently tensile throughout most of the simulation with stresses in the magnitude of  $-10$  MPa (Figures 7e, 8e and 9c). In addition, some of these areas are characterized by the highest predicted shear stresses, in the order of 10 MPa (Figures 7h and 8h). A combination of tensile stresses and relatively high shear stresses could promote fault dilation at shallow level, that is, in the sediment cover where the gas is stored, and thus provide favorable conditions for fluid migration and seepage.

Difficult access to Greenland margins makes challenging the investigation of seafloor methane emissions around Greenland compared to emissions from the formerly glaciated Barents Sea (e.g., Andreassen et al., 2017). However, there are a few studies that document gas seepage and near-surface gas hydrates from the Baffin Bay (e.g., Cramm et al., 2021; MacLean et al., 1981; Punshon et al., 2014) and from other fjord areas along the western coast of Greenland (e.g., Nielsen et al., 2014). The presence of tensile faults and fractures at shallow level, that is, in the sediment cover, in these areas would be favorably dilated for fluid migration and sustained methane release under the predicted glacial stress regime.

The Fram Strait and the Barents Sea Shelf are regions of special interest from both hydro-carbon and climate points of view as faulting is highly associated with the release of methane to the ocean (e.g., Mau et al., 2017; Ostanin et al., 2012; Plaza-Faverola et al., 2015; Waage et al., 2018; Winsborrow et al., 2016). In the Fram Strait area, the release of methane occurs through vertical conduits in hemipelagic sediment known as gas pipes or chimneys (e.g., Bünz et al., 2012; Plaza-Faverola et al., 2015). Buried authigenic carbonate concretions and their response in seismic data reveal episodic release of methane during the Quaternary glaciations (Himmler et al., 2019; Plaza-Faverola et al., 2015). Various sediment proxies indicate that intensified periods of methane release often correlate with the time shortly after the glacial maximum (e.g., Dessandier et al., 2021; Himmler et al., 2019; Schneider et al., 2018). This apparent correlation between methane release and glacial transitions has also been documented from the mid-Norwegian margin where a major event is inferred from ca. 130,000 years (Plaza-Faverola et al., 2011). However, the integration of geophysical observations and sedimentary proxies (dating of events) hints that seepage events are not always correlated with glacial cycles. For instance, along the Vestnesa Ridge, offshore west-Svalbard, there are regions with sedimentary faults that have been releasing methane to the ocean at least for the last 30 years (e.g., Hustoft et al., 2009; Plaza-Faverola et al., 2017; Smith et al., 2014) while adjacent structures closer to the Molloy mid-ocean ridge stopped leaking some 8,000 years ago (e.g., Consolaro et al., 2015).

Analytical tectonic stress modeling suggested that oblique spreading at the Molloy and Knipovich mid-ocean ridges may be generating an abrupt shift in the stress regime from strike-slip dominated closer to the Molloy Deep to a more tensile stress regime toward the northern termination of the Knipovich ridge (Plaza-Faverola & Keiding, 2019). This shift in tectonic stress interestingly correlates spatially with the current distribution of methane seepage (seepage is comprised within the tensile stress field). However, it does not explain why seepage occurred more extensively in the past and suddenly stopped a few thousands of years ago. Plaza-Faverola and Keiding (2019) suggested that a larger impact from glacial stresses following a glacial maximum could have resulted in a more widespread tensile regime in the past (i.e., favoring methane seepage also in the now extinct regions).

Our GIA modeling allows testing this hypothesis. Overall, our models suggest that glacial stresses may have promoted fault dilation and associated gas release in the past (i.e., in the sediments), in the entire Fram Strait. Moreover, it is likely that glacial stresses are contributing to promoting the seepage at present day. The ongoing isostatic rebound forms a complex zone of glacial stresses associated with the Greenland and Barents Sea forebulges that merged in the Fram Strait. The flexure of the Earth's surface along the merged forebulges leads to an

overall N-S stretching. Induced horizontal stresses are dominantly tensile, with the minimum horizontal stress magnitude between  $-4$  MPa and  $-10$  MPa, oriented N-S, parallel to the stretching direction. The combination of relatively high maximum shear stress ( $\sim 3$  MPa) and tensile minimum horizontal stresses ( $\sim -6$  MPa) off the west coast of Svalbard could be enough to promote fault dilation (i.e., in the sediments) and gas leakage from known reservoirs in this region (Daszinnies et al., 2021).

A similar analysis could be done for the western Barents Sea region where extensive areas are covered by seafloor pockmarks and craters, active and extinct, depending on the geological setting and relationship with ice-sheet dynamics (e.g., Andreassen et al., 2017; Chand et al., 2016; Cr mi re et al., 2016; Winsborrow et al., 2016). Unlike the Fram Strait, the Barents Sea was covered by ice, hence it is likely that average stress increase caused by the weight of the ice demoted fracturing or faulting processes in this region during glacial periods. However, in the course that follows the deglaciation of the European ice sheet (from about 15 kyrs BP to present), the drop in confining pressure combined with maximum shear stress that lies between 3 and 6 MPa, could destabilize pre-existing fractures and thus enhance gas seepage activities.

It is important to note that both the Fram Strait and the western Barents Sea regions are in a complex geological setting where several sources of stress (ridge push, transform faults, gravitational potential energy) interact and impact the near surface. Major players to the regional stress field such as ridge push in an extensional geodynamic setting like in the North Atlantic and the Arctic oceans, are known to produce horizontal deviatoric stress at crustal level that lie in the range of 20–40 MPa (Bott, 1991). Further quantification of the effect of glacial stress on near-surface dynamics and Arctic methane release thus requires the analyses of those additional stress sources (Gac et al., 2016; Ghosh et al., 2009; Schiffer et al., 2018). To assess the effect of the regional stress field on faulting, we can assume that the background tectonic stress field does not change during the time of glaciation and deglaciation. This is a reasonable assumption considering that tectonic plates operate on a time scale of millions of years, thus much longer than the time scale of glaciation and deglaciation cycles ( $\sim 10$ – $\sim 100$  kyrs). In future studies, we will establish a background tectonic stress based on geodynamics models of the Fram Strait, onto which the GIA-induced stress field is superposed (e.g., Ivins, 2003; Lund et al., 2009; Steffen et al., 2014; Steffen et al., 2020; Wu et al., 1999; Wu & Hasegawa, 1996).

## 4. Discussions Model Sensitivity and Performance

### 4.1. Sensitivity of the GIA-Induced Stress Field to the Ice Loading Scenario

The ice reconstruction to first order determines both the spatial and temporal evolution of displacements and stress in the model. The present-day solutions of uplift that result from the deglaciation of the Eurasian, North American and Greenland ice sheets were compared with GPS data. We showed that in some areas, our reference model (VL20-175) yields significant differences with these geodetic constraints. In Fennoscandia, for example, the center of the predicted present-day uplift rate is localized 300 km farther north in model VL20-175 than in the GPS observations. If the computed uplift rate field is translated to the southwest (by  $-1.3^\circ$  in latitude and  $-2.5^\circ$  in longitude) the  $\chi^2$  misfit to the GPS observations reduces to 20, compared to 136 before the shift. This suggests that the magnitude of the present-day rebound is well predicted by our model and that the spatial distribution of uplift is strongly dependent on the modeled ice-sheet architecture. The UiT\_2021 ice sheet used in our simulations has the maximum Holocene ice thickness localized over the southern border of the northern Bay of Bothnia, 300 km northward from the maximum uplift observed from GPS data (Figure 4). Other reconstructions of the Fennoscandian ice sheet usually locate the center of the ice cover further south of the Bay of Bothnia or in the Bothnian Sea (e.g., N slund, 2010; Siegert & Dowdeswell, 2004). The predicted uplift pattern from these models usually agrees well with local field constraints. However, the 300 km shift to the northwest of the uplift in Scandinavia has a little influence on Svalbard and around the Barents Sea, the main targets of this study. More importantly, we chose the UiT\_2021 ice sheet model because it is well-resolved over its Arctic segment and has a better fit with relative sea level data around the Barents Sea and Svalbard (Auriac et al., 2016) than other local ice reconstructions (e.g., N slund, 2010; Siegert & Dowdeswell, 2004).

While the extent and chronology of ice-sheet retreat are typically well constrained, the greatest uncertainties in ice sheet reconstructions lie in the thickness of the ice sheet through time (Ely et al., 2021). Recent insights derived through cosmogenic exposure age dating indicate a potential shift in our understanding of the timing and style of the Eurasian ice sheet deglaciation, with indications that ice-sheet thinning was underway soon after

the LGM across southern Fennoscandia (Lane et al., 2020) and the High Arctic (Gjermundsen et al., 2013). Yet, while stress magnitudes might change in future models as ice thicknesses through time become better resolved, the spatial stress patterns and stress orientations induced by GIA are less likely to diverge significantly.

To illustrate this point we compared our UiT\_2021 ice model with the Näslund (2010) reconstruction, in which the Fennoscandian ice sheet is significantly thicker (by about 1,000 m in the Bay of Bothnia at the LGM). Lund and Schmidt (2011) plot the stress magnitude at 18.4 kyrs for Scandinavia, using a flat-earth model (P24) with rheological parameters similar to our TE120 model and the ice reconstruction of (Näslund, 2010). This model predicts glacially induced horizontal stresses at 18.4 kyrs as large as 32 MPa under the center of the ice load (located in the Bay of Bothnia), which is similar to our model VL20-175 at the same time. However, we would expect a more significant difference in the stress magnitude than what we observe considering the 1,000 m discrepancy in the ice thickness between both models. The convergence of both solutions is due to our spherical Earth model that produces horizontal stresses under the center of the ice load that are 10% higher than solutions obtained from a flat Earth model, as in the P24 simulation.

For areas peripheral to the ice sheet and affected by the forebulge, the predicted stress field becomes predominantly sensitive to the timing and duration of maximum loading, rather than its magnitude or precise location. However, for our region of specific interest in the Fram Strait, these potential uncertainties are well mitigated, with maximum ice thickness in the UiT\_2021 reconstruction and over the Svalbard and western Barents Sea reconciling well with cosmogenic exposure ages data (Figure 11 in Patton et al., 2016) and relative sea-level data during deglaciation (Patton et al., 2017). In addition, while the geometry of the ice sheet along the NE Greenland margin is uncertain at the LGM, it has not experienced dramatic changes since then. Therefore, the glacial stress field along the Fram Strait since the LGM is unlikely to diverge significantly under alternative, well-constrained ice-sheet reconstructions for Greenland and Eurasia.

#### 4.2. Sensitivity of the GIA-Induced Stress Field to the Earth Model

Each of the Eurasian, Greenland and North American ice sheet models used in this study were built upon different regional best-fitting Earth models. For example, Patton et al. (2017) shows that the best-fitting earth model for the optimal ice reconstructions over Svalbard, Franz Josef Land, Novaya Zemlya, and Northern Fennoscandia has mantle viscosity and elastic thickness of the Earth lithosphere that are significantly different, illustrating the known rheological heterogeneities across such large domain (see Table 1 in Patton et al., 2017). To avoid including a complex 3D mantle rheology, we settled on a simple viscosity structure (viscosity in the upper and lower mantle is equal to  $1.5 \times 10^{21}$  Pa.s) that was used in regional GIA modeling of Fennoscandia (Lund & Schmidt, 2011; Schmidt et al., 2014) and yield good performance against observational constraints. Lateral variation in the Earth rheology is instead included through the 3D lithosphere structure (e.g., Klemann et al., 2008) that we derive from the elastic thickness of the Earth's Lithosphere model from Tesauro et al. (2013; personal communication). The sensitivity of the GIA simulations and induced stress field to the lithosphere and mantle structure are discussed below.

For simplicity, we did not model the sediment layer at the top of the upper crust whereas it is the location where the methane is stored and escape toward the surface. If we assume that the sediment and methane gas reservoir were already in place prior to 122.8 kyrs, the beginning of our calculation, this sediment layer will be affected by GIA. However, sediments are generally less rigid than crustal rocks underneath and are thus described by lower elastic moduli than for the lithosphere (Guéguen & Palciauskas, 1994; Mavko et al., 2009). Horizontal stresses induced by GIA in the sediment layer will overall be lower (less compressive) in glaciated or formerly glaciated area and higher (less tensile) along the forebulge that forms at the periphery of the ice sheet, in comparison to horizontal stresses found in the Lithosphere underneath.

When analyzing the sensitivity to the Earth model, we have shown that the three tested lithospheric structures (TE60, T120 and VL20-175) essentially yield a similar time and space pattern of the GIA induced stress field. However, we note significant variation in the magnitude of the crustal response to glacial cycles between each model. Overall, we show that the thickness of the elastic lithosphere influences the wavelength of deformation, which agrees with earlier findings (Nield et al., 2018). For example, models that include a thin lithosphere (i.e., TE60 and thin lithospheric region in model VL20-175) produce a deeper subsidence bowl but with horizontal dimensions that are slightly smaller than when including a thicker elastic lithosphere (i.e., TE120). At the

subsurface level, the magnitude of the horizontal stresses at the LGM are 10%–20% higher in models where the lithosphere is 120-km thick (model TE120), whereas a thinner elastic lithosphere leads to more spatial variation of the stress field under and around the changing ice sheet. We found that the velocity field obtained from our three GIA models are similar, however the best fit to the geodetic observation was obtained when including a laterally varying elastic thickness of the Earth's lithosphere. This agrees with previous studies that showed that lateral variations in the lithospheric thickness is important to provide a better fit to GNSS observations, but also because it allows the capture of short-wavelength deformation and a better correction for gravity recovery data (Nield et al., 2018 and references therein).

We did a sensitivity analysis for mantle viscosity while keeping the other rheological parameters (e.g., elastic modulus, elastic thickness of the Earth's lithosphere, density) the same than in model TE120. The first alternative model includes an upper mantle viscosity of  $1.5 \times 10^{21}$  Pa.s and a lower mantle viscosity of  $1.5 \times 10^{22}$  Pa.s (see Figures D1 and D2). As expected, we note that the viscosity of the mantle controls the rate of deformation so that GIA induced stresses, in this example, build up or decay slower during glacial advances and retreat, respectively, when the viscosity is higher. An increase in the viscosity of the lower mantle by one order of magnitude leads to glacial stresses that are 20%–25% lower under the center of the ice sheet at the LGM than for models TE120 (Figures D1a, D1d, and D1g). At present, residual glacial stresses are higher in formerly glaciated regions than in our model TE120 by about 30%–40% (Figure D2a, D2d, and D2g). Note that the spatial distribution of both deformation and stresses induced by glacial cycles are similar to the models presented in this study. In a second example, we test the viscosity structure presented in Lambeck et al. (2017) where the upper and lower mantle viscosity equal  $5.1 \times 10^{20}$  and  $1.3 \times 10^{22}$  Pa.s respectively, while keeping the elastic thickness of the Earth's lithosphere constant and equal to 120 km (as in model TE120). We show in Figure D3 that our model that includes the Lambeck viscosity structure produce glacial stresses that are overall 10%–15% larger than for model TE120 at the LGM and in glaciated regions. We note that the lower upper mantle viscosity has induced a faster rebound of Northern Europe (Figures D4a, D4d, and D4g) since the beginning of the Holocene deglaciation, in comparison to model TE120 (Figures C1a, C1d, and C1g). Hence, the maximum shear stress and the horizontal stresses today have almost fully vanished in this region. In comparison, model TE120 have residual  $\sigma_H$  and  $\tau_{max}$  in Northern Europe of about 5–8 and 0–3 MPa respectively at present time (Figures C2 and C3).

### 4.3. Effect of Tectonic Processes, Temperature Anomaly and Plate Boundary on the GIA Solution Over the Fram Strait and Svalbard Regions

Interestingly, our models and previous GIA studies show that there is a general underestimation of the uplift rate in the Svalbard region (Auriac et al., 2016 and references therein). We argue that the mismatch between the computed present-day uplift and GPS measurement in that area is most likely due to a combination of mechanisms that are generally not considered in GIA models:

- Temperature anomaly: Interpretation of seismic tomography models and magneto telluric investigations have revealed a strong temperature anomaly in the upper mantle of the North Atlantic (Minakov, 2018 and reference therein; Selway et al., 2020), probably linked with the Icelandic and Jan Mayen hotspots. Results indicate an average excess mantle temperature under Svalbard (40°C–100°C) compared to the central Barents Sea. That would correspond to a layer of viscosity  $\sim 10^{18}$  Pa.s in the uppermost mantle and a layer of viscosity  $\sim 10^{20}$  Pa.s in the underlying lower mantle (Selway et al., 2020). These values are more than two orders of magnitude lower than what is typically used in GIA studies (including ours) for the Svalbard area (Auriac et al., 2016; Patton et al., 2017). Model predictions that include such a weak viscosity structure could yield a faster response, hence higher uplift rate, to present-day ice mass loss (not included in our model) in Svalbard.
- Background tectonic stresses: Modeling of the gravitational potential energy in the Barents Sea region suggests that the ridge push force from the ocean spreading of the North Atlantic ridges is large enough to cause contraction in the Barents Sea shelf (Gac et al., 2016, 2020). The net horizontal forces that result from this mechanism are most likely important enough to induce a general uplift of the area comprised between the North Atlantic ridges and the East of the Barents Sea (including Svalbard). However, the present-day contribution of this process to the measured uplift over Svalbard remains unconstrained.
- Plate boundary (Mid Atlantic ridge): One other mechanism that we did not consider in this modeling study is the influence of the plate boundary (i.e., the North Atlantic ridge) on the GIA-induced motion. We showed throughout this paper that the GIA of each glaciated (or formerly glaciated) area is primarily controlled by

the regional Earth rheology and respective ice sheets. However, in a place such as the Fram Strait, the close vicinity with the Greenland, North American and Eurasian ice sheets imply an influence of all three ice bodies on the regional GIA. Considering that the mid-Atlantic ridge crosses the Fram Strait, we should consider how the plate boundary may affect the GIA induced displacement. In Klemann et al. (2008), the authors tested the effect of a plate boundary on GIA-induced motion by modeling it as a low viscosity zone. They showed that the low viscosity zone behaves as a free-slip boundary, effectively decoupling horizontal motion at crustal level from one side of the plate boundary to the other. However, vertical motion caused by the weight of the ice sheet through the crust and mantle was relatively little influenced by the presence of the plate boundary. The decoupling of horizontal displacement between one side of the ridge to the other could have an important influence on stress perturbation i.e., caused by GIA through the lithosphere, especially in the horizontal plane. It is also possible that the slipping boundary yields to relaxation of shear stresses across the Fram Strait, potentially relieving shear on fault there. This will be the matter of further study.

## 5. Conclusions

We modeled the evolution in space and time of the GIA induced stress field caused by the weight of the North American, Eurasian and Greenland ice sheets from the Eemian to present. We derived the stress field generated by the ice sheets in the northern hemisphere from a GIA model that: (a) accounts for a 3D spherical Earth; and (b) assumes a quasi-static and visco-elastic Earth i.e., in hydrostatic equilibrium. Our major findings are summarized below:

1. While the overall stress solution is strongly dependent on the ice load scenario and the rheological parameters used, the general pattern of stress distribution is similar between Earth models. We show that models that include a thick elastic lithosphere have glacial stresses of slightly higher magnitude, whereas models that include a thin elastic lithosphere leads to more spatial variation of the stress field under and around the ice sheets.
2. At the LGM (23 kyrs BP) the maximum horizontal stress ranges from 20 to 25 MPa in the glaciated regions of Northern Europe to 35–40 MPa at the center of Greenland. Along the peripheral forebulges the horizontal stresses are dominantly tensile and  $\sigma_H$  averages  $-4$  to  $-8$  MPa. At present time, formerly glaciated regions like Northern Europe are actively rebounding and horizontal stresses have decreased by a factor 3 to 4 since the LGM. In Northern Europe, the maximum shear stress reaches a peak during the deglaciation of the ice with magnitude as high as 5–10 MPa.
3. In our reference model VL20-175, the merging of the Greenland and Barents Sea forebulges over the Fram Strait forms a complex stress topography where the maximum horizontal stress at present is dominantly tensile ( $\sim 0$  to  $-4$  MPa) and oriented E-W. The association of relatively high shear stress ( $\sim 3$ – $5$  MPa) and tensile horizontal stresses along the well-known seepage sites off the west-Svalbard coast (i.e., Vestnesa ridge) could be sufficient to promote fault reactivation and dilation that favor gas leakage from gas reservoirs. A more tensile stress regime in the Fram Strait as during the LGM would have more impact on pre-existing faults in methane seepage reservoirs.
4. The Barents Sea region was under a glacial stress field characterized by maximum horizontal stress and maximum shear stresses as large as 20–25 and 5–8 MPa, respectively, during the last glaciation. It is likely that faulting processes were hindered during glaciation period, however the drop in the confining stress that follows the melting of the North European ice sheet could promote reactivation of pre-existing fault and thus enhance gas seepage activities.



Appendix A: Ice Model Characteristic (Greenland Huy3 and Northern Europe UiT\_2021)

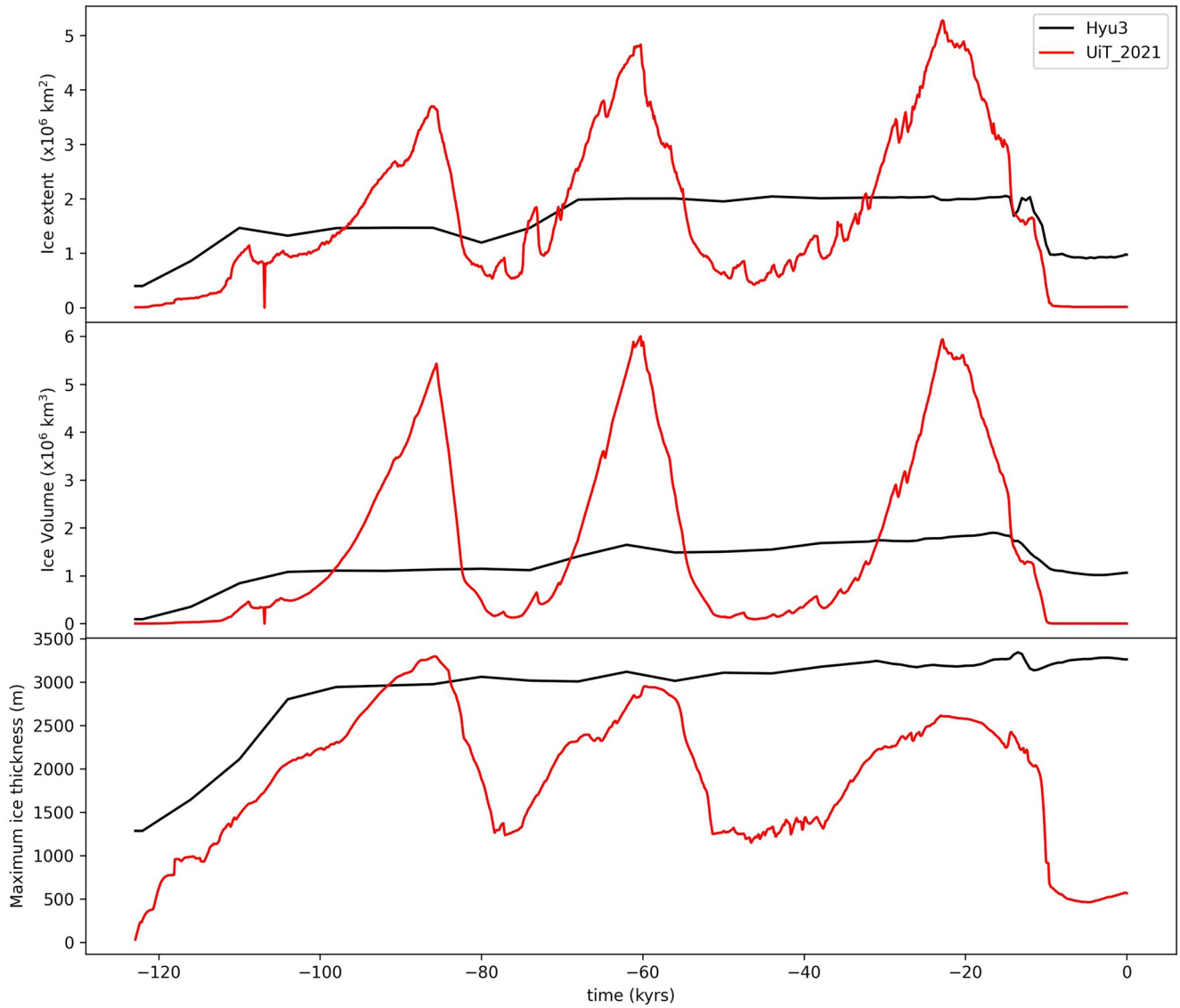


**Figure A1.** Ice model characteristics: Areal extent, volume and maximum ice thickness for model Huy3 (black—Greenland ice sheet) and model UiT2021 (red—Weichselian ice sheet).

Appendix B: Vertical Surface Displacement and GIA Induced Stresses at the LGM (23 kyrs BP) for All Tested Earth Models TE60, TE120, and VL20-175

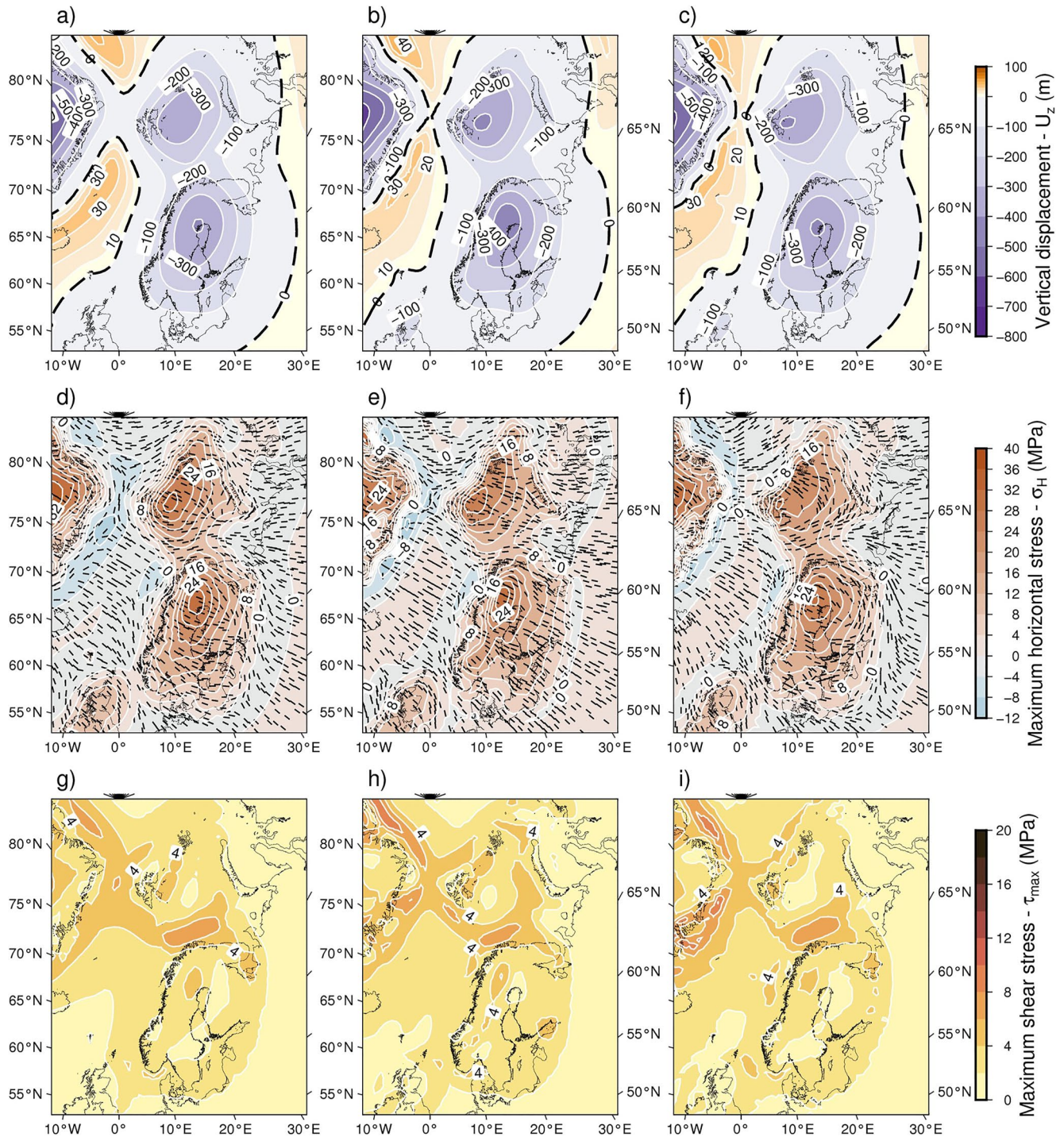
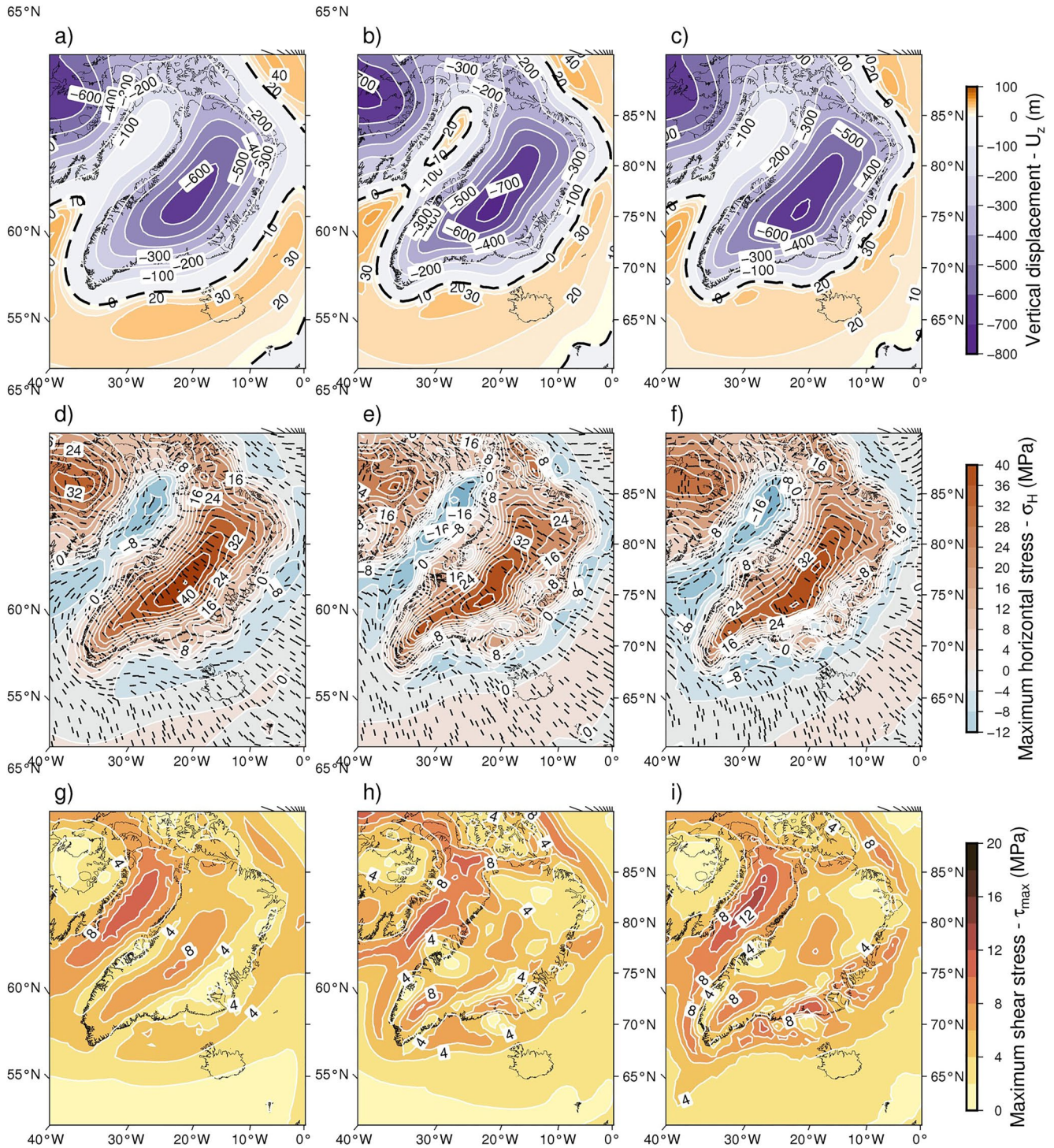
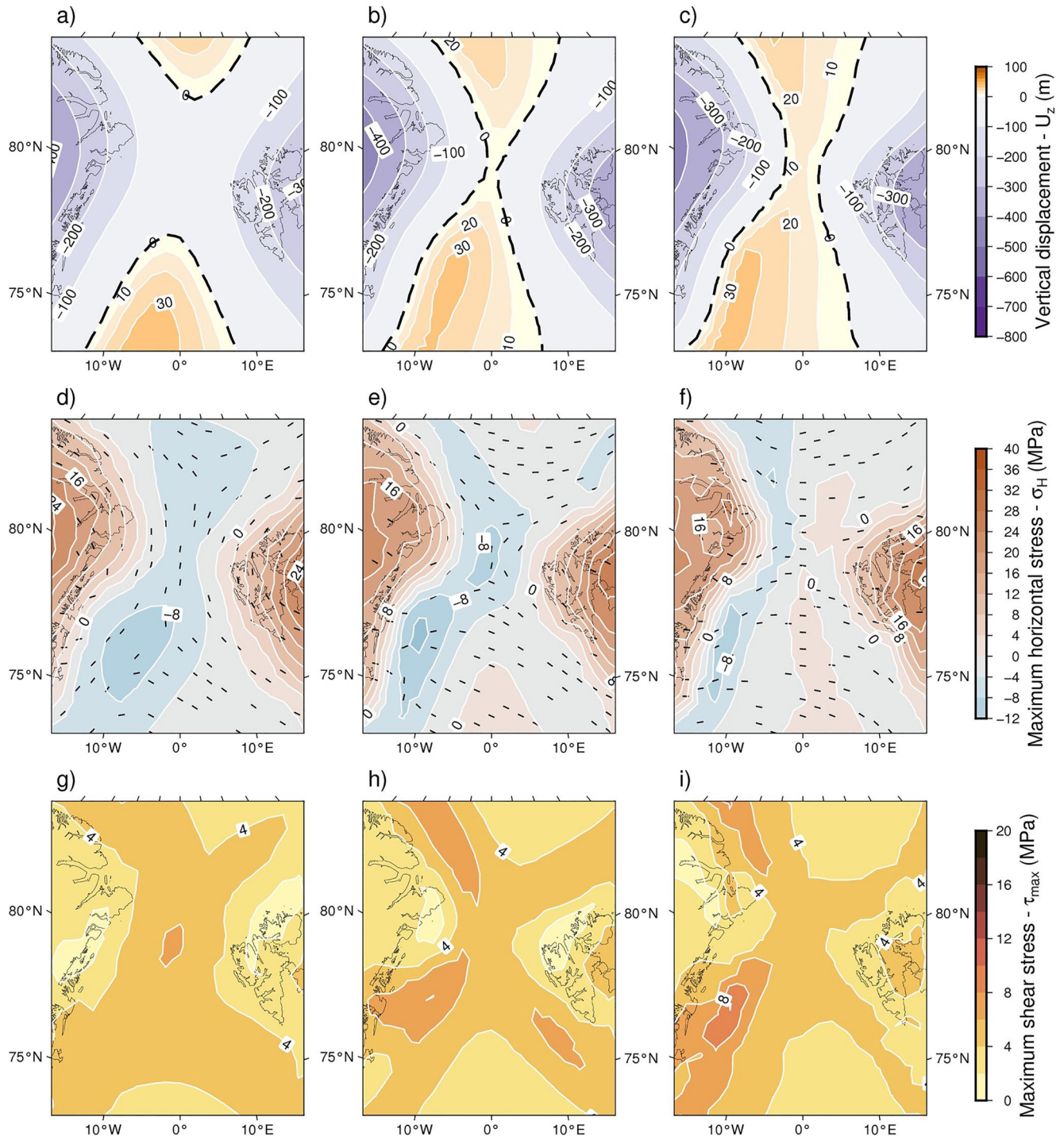


Figure B1. Maps of (a–c) the vertical surface displacement ( $U_z$ ), (d–f) the maximum horizontal stress ( $\sigma_H$ ) and (g–i) the maximum shear stress ( $\tau_{max}$ ). Solutions are computed at the LGM (23kyrs BP) over Northern Europe and at 2.5 km depth for model (a, d, g) TE120, (b, e, h) TE60 and (c, f, i) VL20-175.



**Figure B2.** Maps of (a–c) the vertical surface displacement ( $U_z$ ), (d–f) the maximum horizontal stress ( $\sigma_H$ ) and (g–i) the maximum shear stress ( $\tau_{max}$ ). Solutions are computed at the LGM (23 kyrs BP) over Greenland and at 2.5 km depth for model (a, d, g) TE120, (b, e, h) TE60 and (c, f, i) VL20-175.



**Figure B3.** Maps of (a–c) the vertical surface displacement ( $U_z$ ), (d–f) the maximum horizontal stress ( $\sigma_H$ ) and (g–i) the maximum shear stress ( $\tau_{max}$ ). Solutions are computed at the LGM (23 kys BP) over the Fram Strait and at 2.5 km depth for model (a, d, g) TE120, (b, e, h) TE60 and (c, f, i) VL20-175.

Appendix C: Vertical Surface Displacement and GIA Induced Stresses at Present Time for All Earth Models

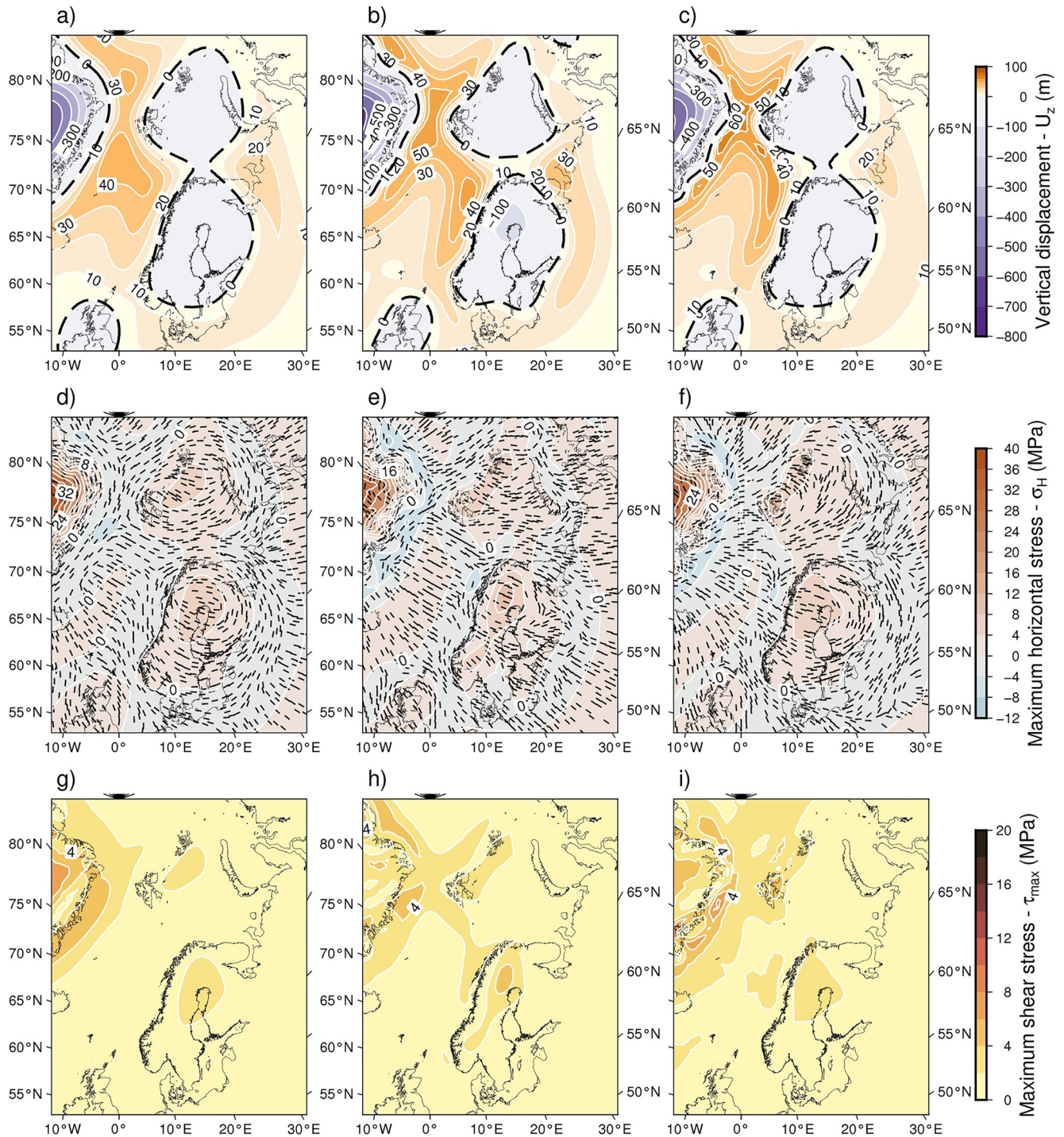
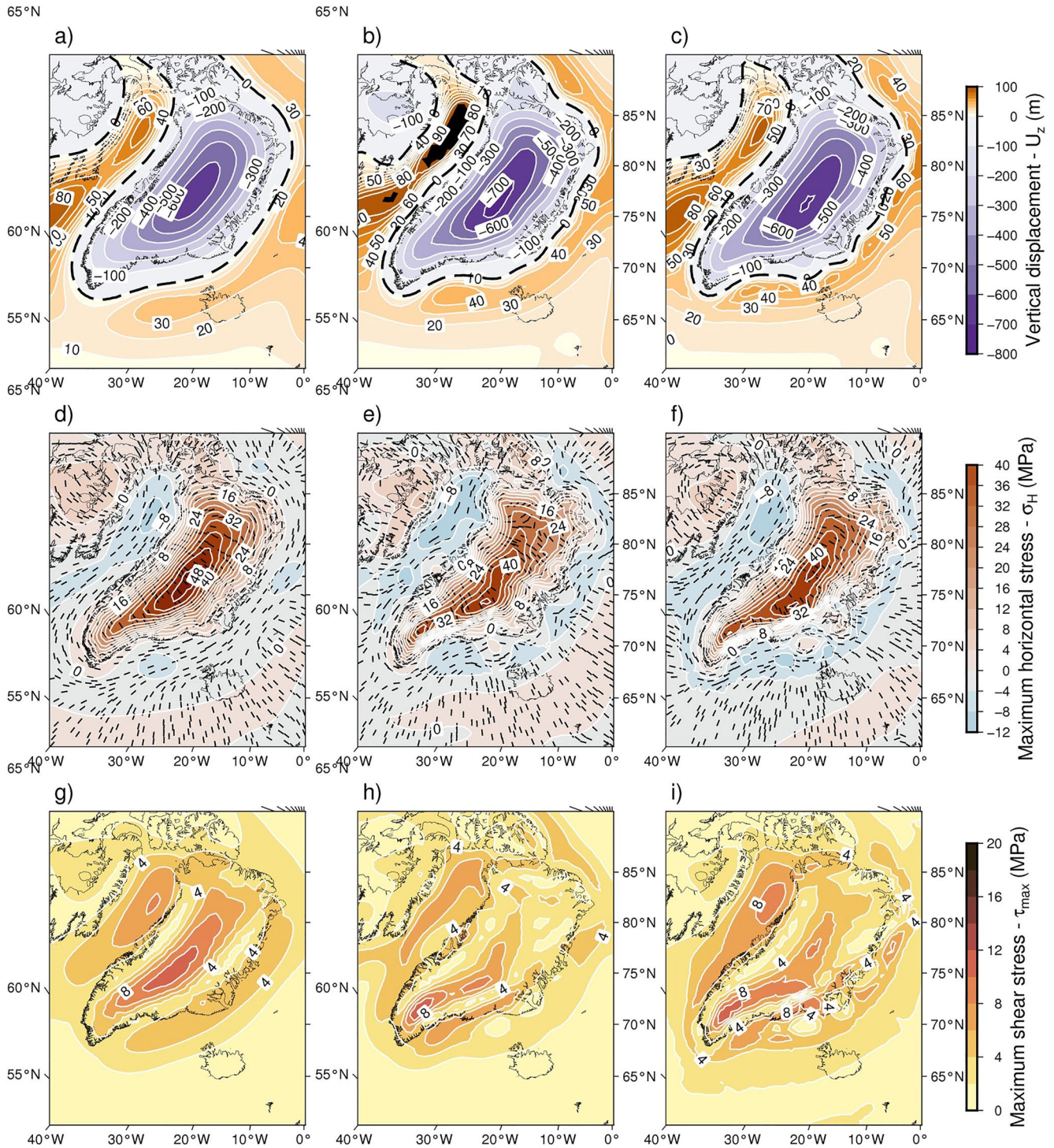
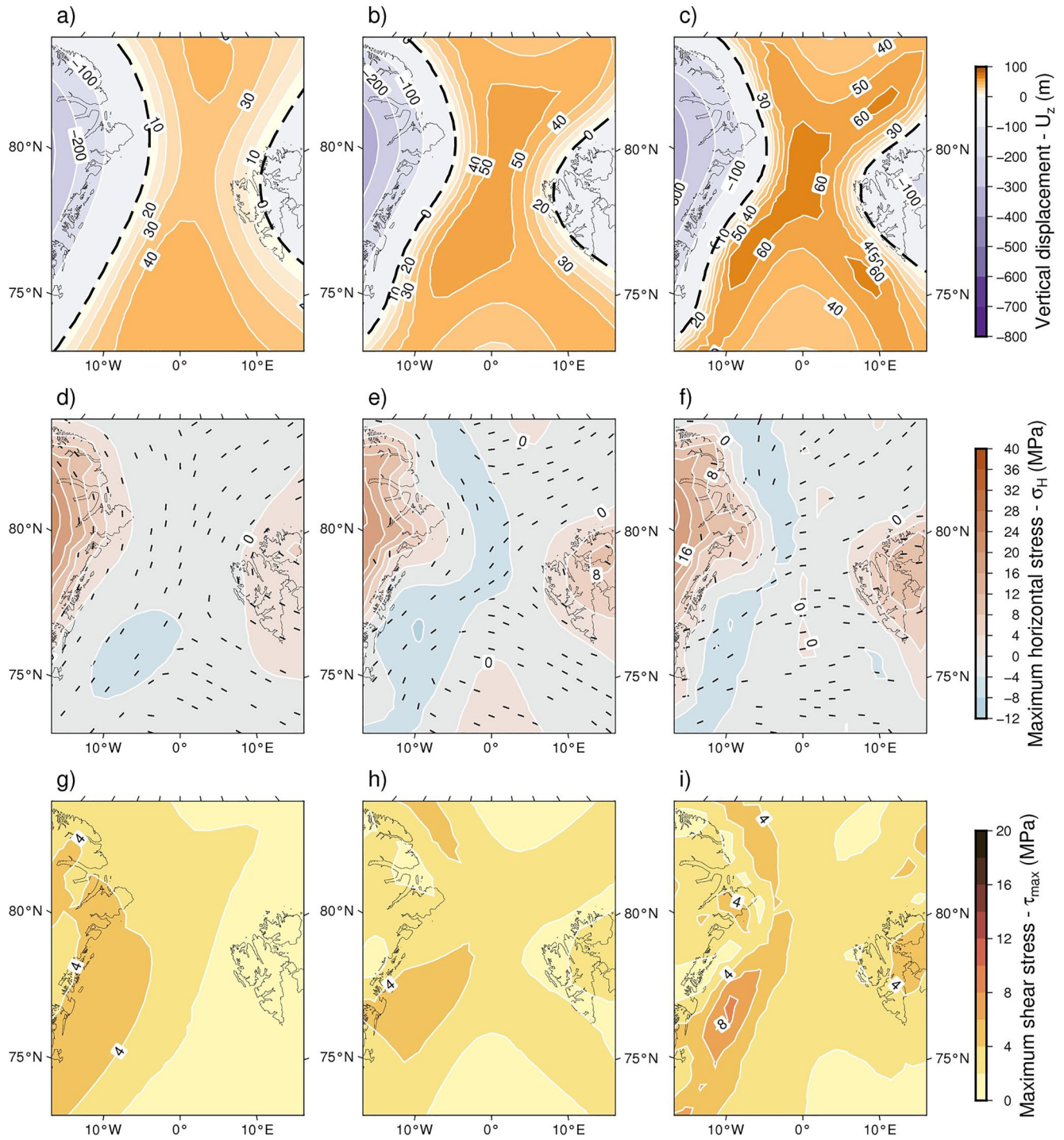


Figure C1. Present-day maps of (a–c) the vertical displacement ( $U_z$ ), (d–f) the maximum horizontal stress ( $\sigma_H$ ) and (g–i) the maximum shear stress ( $\tau_{max}$ ). Solutions are computed over Northern Europe and at 2.5 km depth for model (a, d, g) TE120, (b, e, h) TE60 and (c, f, i) VL20-175.



**Figure C2.** Present-day maps of (a–c) the vertical surface displacement ( $U_z$ ), (d–f) the maximum horizontal stress ( $\sigma_H$ ) and (g–i) the maximum shear stress ( $\tau_{max}$ ). Solutions are computed over Greenland and at 2.5 km depth for model (a, d, g) TE120, (b, e, h) TE60 and (c, f, i) VL20-175.



**Figure C3.** Present-day maps of (a–c) the vertical surface displacement ( $U_z$ ), (d–f) the maximum horizontal stress ( $\sigma_H$ ) and (g–i) the maximum shear stress ( $\tau_{max}$ ). Solutions are computed over the Fram Strait and at 2.5 km depth for model (a, d, g) TE120, (b, e, h) TE60 and (c, f, i) VL20-175.

Appendix D: Vertical Surface Displacement and Glacial Isostatic Adjustment Induced Stresses at the Last Glacial Maximum and Present Time for Model TE120 With Alternative Viscosity Structures

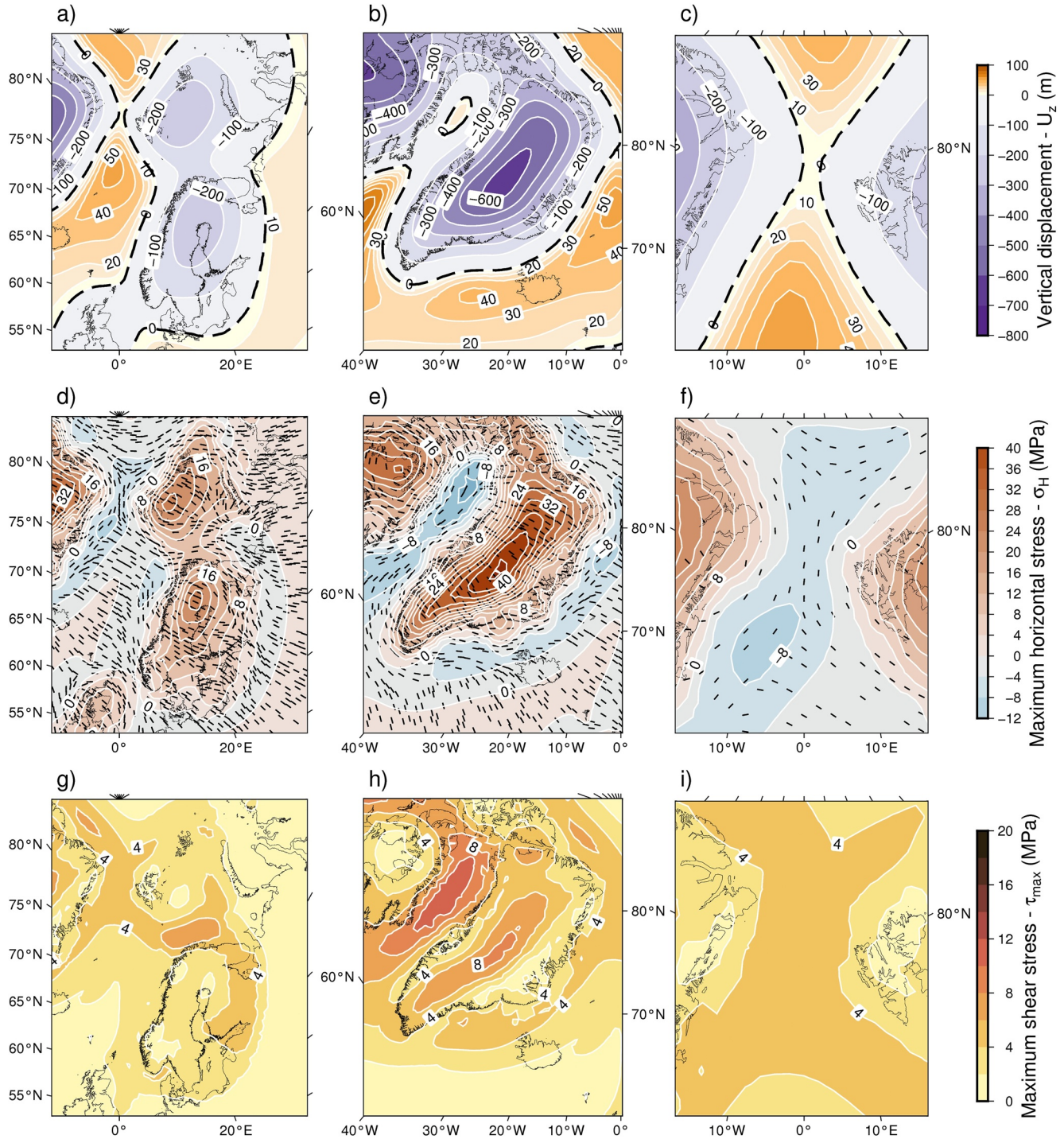


**Figure D1.** Maps of (a–c) the vertical displacement at surface level, (d–f) the maximum horizontal stress (at 2.5 km depth) and (g–i) the maximum shear stress (at 2.5 km depth) computed for model TE120 with the alternative viscosity structure (upper and lower mantle viscosity equal to  $1.5 \times 10^{21}$  and  $1.5 \times 10^{22}$  Pa.s respectively) at the Last Glacial Maximum (LGM) (23 kyrs BP), over (a, d, g) Fennoscandia, (b, e, h) Greenland and (c, f, i) the Fram Strait. The dashed lines define the 0 m contour the subsidence bowls.



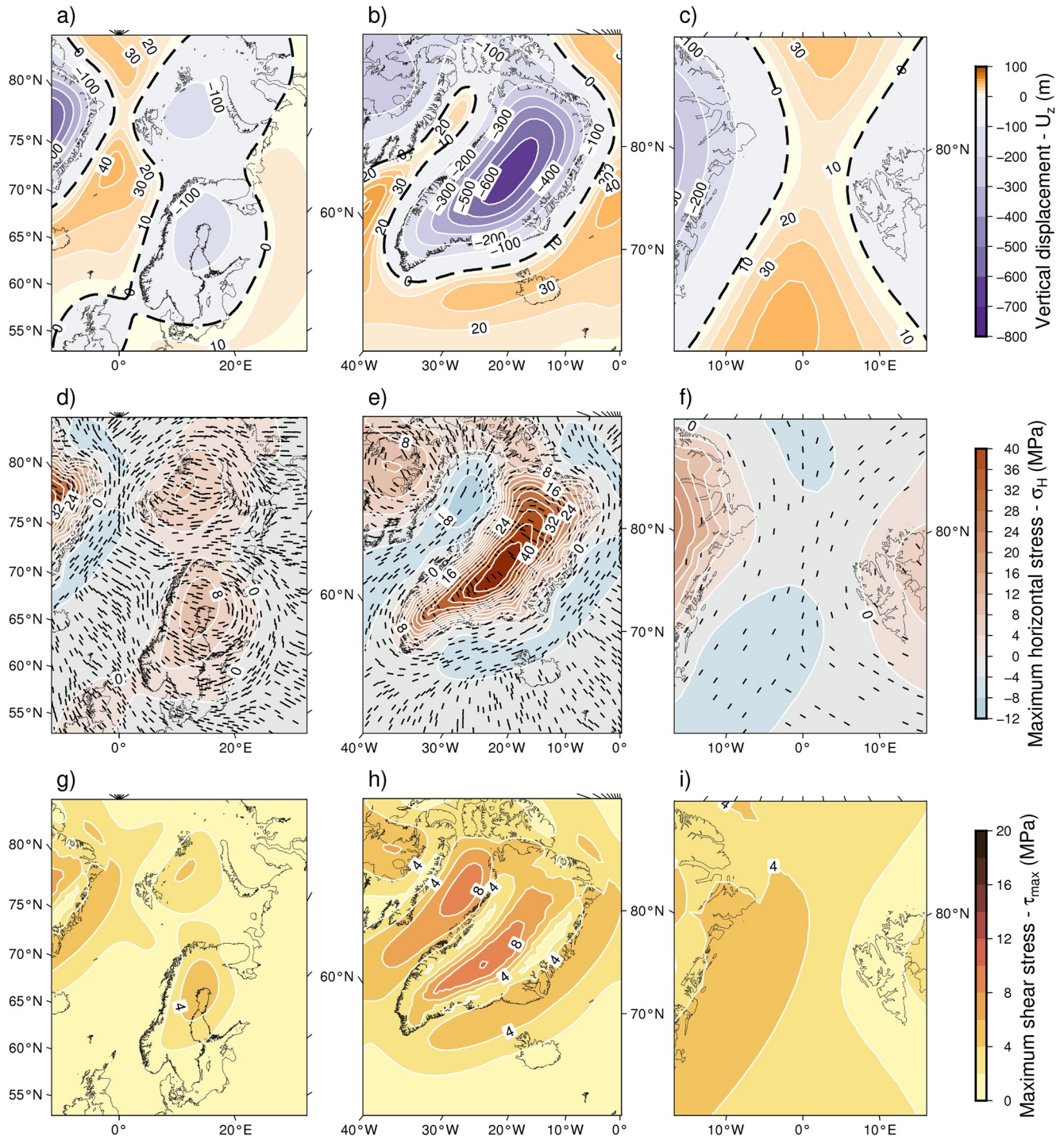


**Figure D2.** Maps of (a–c) the vertical displacement at surface level, (d–f) the maximum horizontal stress (at 2.5 km depth) and (g–i) the maximum shear stress (at 2.5 km depth) computed for model TE120 with the alternative viscosity structure (upper and lower mantle viscosity equal to  $1.5 \times 10^{21}$  and  $1.5 \times 10^{22}$  Pa.s respectively) at present time over (a, d, g) Fennoscandia, (b, e, h) Greenland and (c, f, i) the Fram Strait. The dashed lines define the 0 m contour the subsidence bowls.

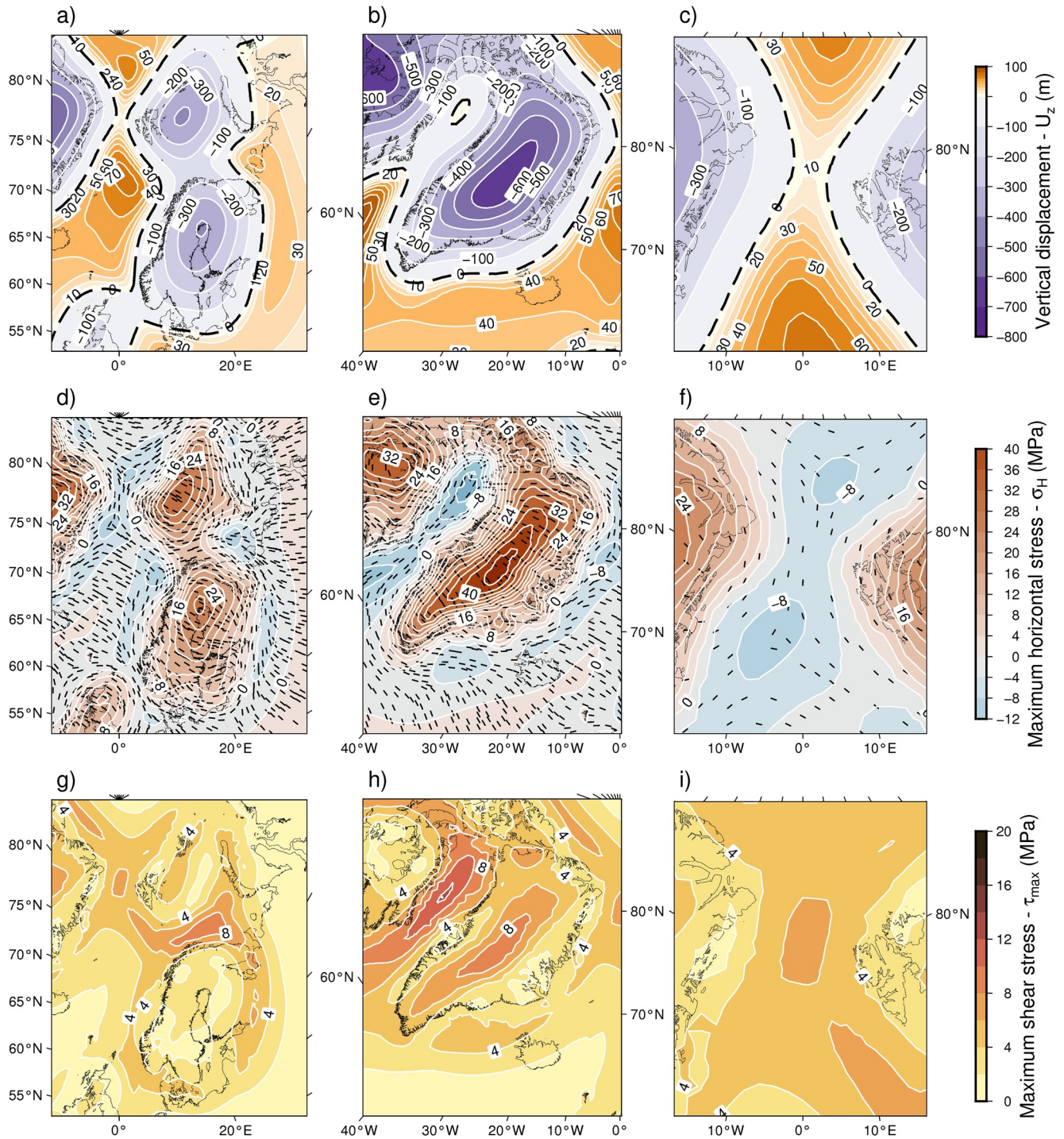


**Figure D3.** Maps of (a–c) the vertical displacement at surface level, (d–f) the maximum horizontal stress (at 2.5 km depth) and (g–i) the maximum shear stress (at 2.5 km depth) computed for model TE120 with the Lambeck alternative viscosity structure (upper and lower mantle viscosity equal to  $5.1 \times 10^{20}$  and  $1.3 \times 10^{22}$  Pa.s respectively) at the Last Glacial Maximum (LGM) (23 kyrs BP), over (a, d, g) Fennoscandia, (b, e, h) Greenland and (c, f, i) the Fram Strait. The dashed lines define the 0 m contour the subsidence bowls.

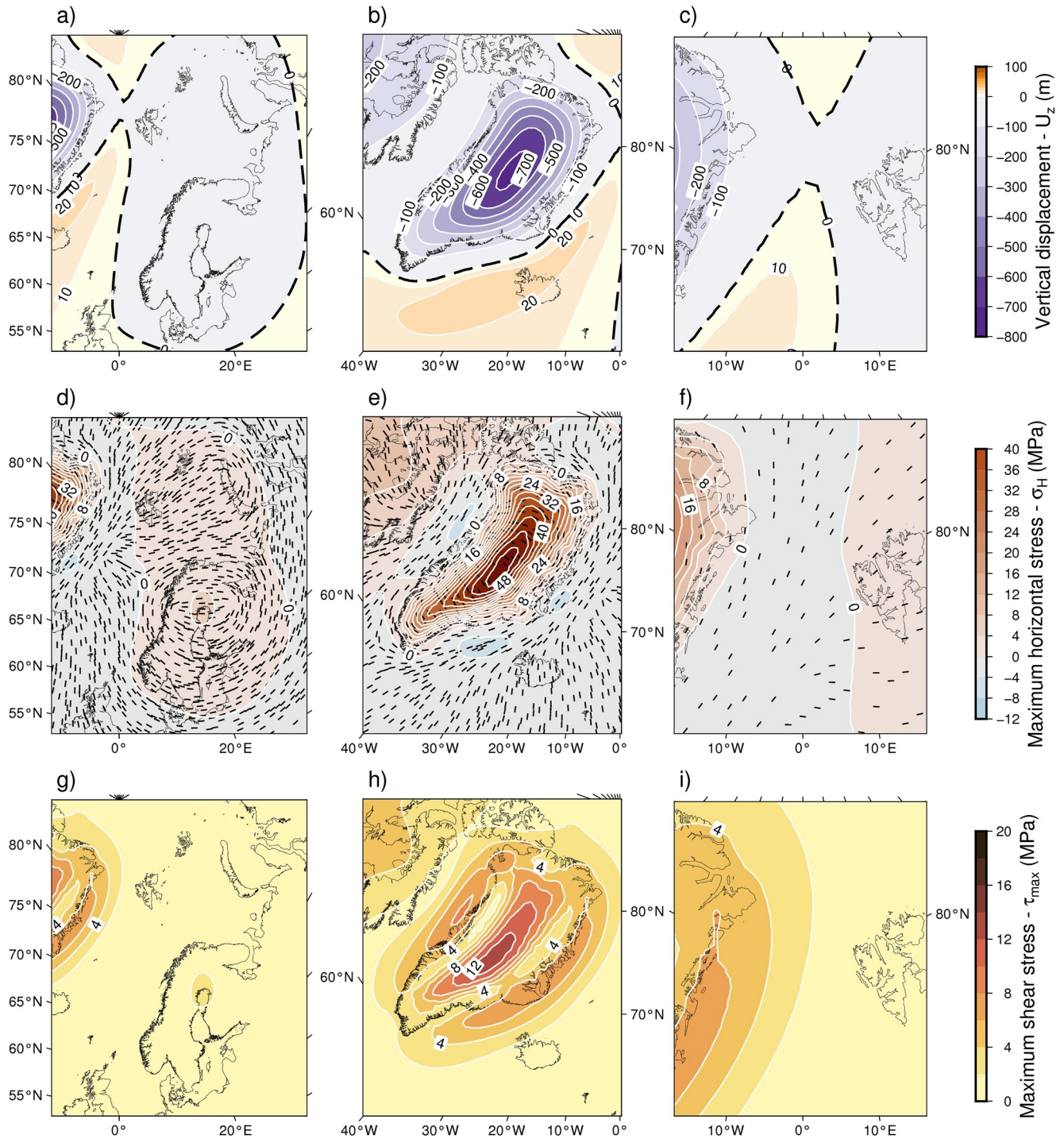


**Figure D4.** Maps of (a–c) the vertical displacement at surface level, (d–f) the maximum horizontal stress (at 2.5 km depth) and (g–i) the maximum shear stress (at 2.5 km depth) computed for model TE120 with the Lambeck alternative viscosity structure (upper and lower mantle viscosity equal to  $5.1 \times 10^{20}$  and  $1.3 \times 10^{22}$  Pa.s respectively) at present time and over (a, d, g) Fennoscandia, (b, e, h) Greenland and (c, f, i) the Fram Strait. The dashed lines define the 0 m contour the subsidence bowls.

## Data Availability Statement

Stress (maximum horizontal and shear), vertical surface displacement and velocity data computed from each our GIA models are archived and available online at the following URL: <https://dataverse.no/dataset.xhtml?persistentId=doi:10.18710/QBSWEH>.

## Acknowledgments

This study is part of the SEAMSTRESS project. It is supported by starting grants from the Tromsø Research Foundation (TFS) and the Research Council of Norway (Grant 287865) awarded to A. Plaza-Faverola. The work is also supported by the Research Council of Norway through its Centers of Excellence funding scheme, project 223259. We would like to acknowledge Benoit Lecavalier for kindly sharing his ice reconstruction of Greenland. We also acknowledge Magdala Tesaro for providing data of the elastic thickness of the Earth's lithosphere for the Northern hemisphere.

## References

- Andreassen, K., Hubbard, A., Winsborrow, M., Patton, H., Vadakkepuliambatta, S., Plaza-Faverola, A., et al. (2017). Massive blow-out craters formed by hydrate-controlled methane expulsion from the Arctic seafloor. *Science*, 356(6341), 948–953. <https://doi.org/10.1126/SCIENCE.AAL4500>
- Argus, D. F., Peltier, W. R., Drummond, R., & Moore, A. W. (2014). The Antarctica component of postglacial rebound model ICE-6G\_C (VM5a) based on GPS positioning, exposure age dating of ice thicknesses, and relative sea level histories. *Geophysical Journal International*, 198(1), 537–563. <https://doi.org/10.1093/gji/ggu140>
- Auriac, A., Whitehouse, P. L., Bentley, M. J., Patton, H., Lloyd, J. M., & Hubbard, A. (2016). Glacial isostatic adjustment associated with the Barents Sea ice sheet: A modelling inter-comparison. *Quaternary Science Reviews*, 147, 122–135. <https://doi.org/10.1016/j.quascirev.2016.02.011>
- Bängtsson, E., & Lund, B. (2008). A comparison between two solution techniques to solve the equations of glacially induced deformation of an elastic Earth. *International Journal for Numerical Methods in Engineering*, 75(4), 479–502. <https://doi.org/10.1002/nme.2268>
- Bott, M. H. P. (1991). Ridge push and associated plate interior stress in normal and hot spot regions. *Tectonophysics*, 200(1–3), 17–32. [https://doi.org/10.1016/0040-1951\(91\)90003-B](https://doi.org/10.1016/0040-1951(91)90003-B)
- Bünz, S., Polyanov, S., Vadakkepuliambatta, S., Consolaro, C., & Mienert, J. (2012). Active gas venting through hydrate-bearing sediments on the Vestnesa Ridge, offshore W-Svalbard. *Marine Geology*, 332–334, 189–197. <https://doi.org/10.1016/j.margeo.2012.09.012>
- Cathles, L. M. I. (1972). The viscosity of the Earth's mantle. Retrieved from <https://elibrary.ru/item.asp?id=7016139>
- Chand, S., Thorsnes, T., Rise, L., Brunstad, H., & Stoddart, D. (2016). Pockmarks in the SW Barents Sea and their links with iceberg ploughmarks. *Geological Society, London, Memoirs*, 46(1), 295–296. <https://doi.org/10.1144/M46.23>
- COMSOL. (2022). In COMSOL-A. B. (Ed.), *COMSOL Multiphysics*®. Retrieved from [www.comsol.com](http://www.comsol.com)
- Consolaro, C., Rasmussen, T. L., Panieri, G., Mienert, J., Bünz, S., & Szttybor, K. (2015). Carbon isotope ( $\delta^{13}\text{C}$ ) excursions suggest times of major methane release during the last 14 kyr in Fram Strait, the deep-water gateway to the Arctic. *Climate of the Past*, 11(4), 669–685. <https://doi.org/10.5194/cp-11-669-2015>
- Cramm, M. A., Neves, B. d. M., Manning, C. C. M., Oldenburg, T. B. P., Archambault, P., Chakraborty, A., et al. (2021). Characterization of marine microbial communities around an Arctic seabed hydrocarbon seep at Scott Inlet, Baffin Bay. *Science of The Total Environment*, 762, 143961. <https://doi.org/10.1016/j.scitotenv.2020.143961>
- Crémère, A., Lepland, A., Chand, S., Sahy, D., Condon, D. J., Noble, S. R., et al. (2016). Timescales of methane seepage on the Norwegian margin following collapse of the Scandinavian ice sheet. *Nature Communications*, 7(1), 11509. <https://doi.org/10.1038/ncomms11509>
- Daszyniecki, M., Plaza-Faverola, A., Sylta, Ø., Bünz, S., Mattingsdal, R., Tømmerås, A., & Knies, J. (2021). The Plio-Pleistocene seepage history off Western Svalbard inferred from 3D petroleum systems modelling. *Marine and Petroleum Geology*, 128, 105023. <https://doi.org/10.1016/j.marpetgeo.2021.105023>
- Dessandier, P. A., Knies, J., Plaza-Faverola, A., Labrousse, C., Renoult, M., & Panieri, G. (2021). Ice-sheet melt drove methane emissions in the Arctic during the last two interglacials. *Geology*, 49(7), 799–803. <https://doi.org/10.1130/G48580.1>
- Dugan, B., & Sheahan, T. C. (2012). Offshore sediment overpressures of passive margins: Mechanisms, measurement, and models. *Reviews of Geophysics*, 50(3), RG3001. <https://doi.org/10.1029/2011rg000379>
- Dziewonski, A. M., & Anderson, D. L. (1981). Preliminary reference Earth model. *Physics of the Earth and Planetary Interiors*, 25(4), 297–356. [https://doi.org/10.1016/0031-9201\(81\)90046-7](https://doi.org/10.1016/0031-9201(81)90046-7)
- Ely, J. C., Clark, C. D., Hindmarsh, R. C. A., Hughes, A. L. C., Greenwood, S. L., Bradley, S. L., et al. (2021). Recent progress on combining geomorphological and geochronological data with ice sheet modelling, demonstrated using the last British–Irish ice sheet. *Journal of Quaternary Science*, 36(5), 946–960. <https://doi.org/10.1002/jqs.3098>
- Étioppe, G., Milkov, A. V., & Derbyshire, E. (2008). Did geologic emissions of methane play any role in Quaternary climate change? *Global and Planetary Change*, 61(1), 79–88. <https://doi.org/10.1016/j.gloplacha.2007.08.008>
- Étioppe, G., & Sherwood Lollar, B. (2013). Abiotic methane on Earth. *Reviews of Geophysics*, 51(2), 276–299. <https://doi.org/10.1002/rog.20011>
- Gac, S., Klitzke, P., Minakov, A., Faleide, J. I., & Scheck-Wenderoth, M. (2016). Lithospheric strength and elastic thickness of the Barents Sea and Kara Sea region. *Tectonophysics*, 691, 120–132. <https://doi.org/10.1016/j.tecto.2016.04.028>
- Gac, S., Minakov, A., Shephard, G. E., Faleide, J. I., & Planke, S. (2020). Deformation analysis in the Barents Sea in relation to Paleogene transpression along the Greenland-Eurasia plate boundary. *Tectonics*, 39(10), e2020TC006172. <https://doi.org/10.1029/2020TC006172>
- Ghosh, A., Holt, W. E., & Flesch, L. M. (2009). Contribution of gravitational potential energy differences to the global stress field. *Geophysical Journal International*, 179(2), 787–812. <https://doi.org/10.1111/j.1365-246X.2009.04326.X>
- Gjermundsen, E. F., Briner, J. P., Akçar, N., Salvigsen, O., Kubik, P., Gantert, N., & Holmes, A. (2013). Late Weichselian local ice dome configuration and chronology in Northwestern Svalbard: Early thinning, late retreat. *Quaternary Science Reviews*, 72, 112–127. <https://doi.org/10.1016/j.quascirev.2013.04.006>
- Guéguen, Y., & Palciauskas, V. (1994). *Introduction to the physics of rocks*. Princeton University Press.
- Hampel, A., & Hetzel, R. (2006). Response of normal faults to glacial-interglacial fluctuations of ice and water masses on Earth's surface. *Journal of Geophysical Research*, 111(B6). <https://doi.org/10.1029/2005jb004124>
- Himmeler, T., Sahy, D., Martma, T., Bohrmann, G., Plaza-Faverola, A., Bünz, S., et al. (2019). A 160, 000-year-old history of tectonically controlled methane seepage in the Arctic. *Science Advances*, 5(8). <https://doi.org/10.1126/SCIADV.AAW1450>
- Hooper, A., Ófeigsson, B., Sigmundsson, F., Lund, B., Einarsson, P., Geirsson, H., & Sturkell, E. (2011). Increased capture of magma in the crust promoted by ice-cap retreat in Iceland. *Nature Geoscience*, 4(11), 783–786. <https://doi.org/10.1038/ngeo1269>
- Hornbach, M. J., Saffer, D. M., & Steven Holbrook, W. (2004). Critically pressured free-gas reservoirs below gas-hydrate provinces. *Nature*, 427(6970), 142–144. <https://doi.org/10.1038/nature02172>
- Hustoft, S., Bünz, S., Mienert, J., & Chand, S. (2009). Gas hydrate reservoir and active methane-venting province in sediments on <20 Ma young oceanic crust in the Fram Strait, offshore NW-Svalbard. *Earth and Planetary Science Letters*, 284(1), 12–24. <https://doi.org/10.1016/j.epsl.2009.03.038>

- Ivins, E. R. (2003). Glacial isostatic stress shadowing by the Antarctic ice sheet. *Journal of Geophysical Research*, *108*(B12), 2560. <https://doi.org/10.1029/2002jb002182>
- Jakovlev, A. V., Bushenkova, N. A., Koulakov, I. Y., & Dobretsov, N. L. (2012). Structure of the upper mantle in the Circum-Arctic region from regional seismic tomography. *Russian Geology and Geophysics*, *53*(10), 963–971. <https://doi.org/10.1016/j.rgg.2012.08.001>
- Johnston, P., Wu, P., & Lambeck, K. (1998). Dependence of horizontal stress magnitude on load dimension in glacial rebound models. *Geophysical Journal International*, *132*(1), 41–60. <https://doi.org/10.1046/j.1365-246x.1998.00387.x>
- Jull, M., & McKenzie, D. (1996). The effect of deglaciation on mantle melting beneath Iceland. *The Effect of Deglaciation on Mantle Melting Beneath Iceland*, *101*(B10), 21815–21828. <https://doi.org/10.1029/96jb01308>
- Kendall, R. A., Mitrovica, J. X., & Milne, G. A. (2005). On post-glacial sea level—II. Numerical formulation and comparative results on spherically symmetric models. *Geophysical Journal International*, *161*(3), 679–706. <https://doi.org/10.1111/j.1365-246X.2005.02553.x>
- Khan, S. A., Sasgen, I., Bevis, M., Van Dam, T., Bamber, J. L., Willis, M., et al. (2016). Geodetic measurements reveal similarities between post-Last Glacial Maximum and present-day mass loss from the Greenland ice sheet. *Science Advances*, *2*(9), e1600931. <https://doi.org/10.1126/sciadv.1600931>
- Kierulf, H. P., Steffen, H., Barletta, V. R., Lidberg, M., Johansson, J., Kristiansen, O., & Tarasov, L. (2021). A GNSS velocity field for geophysical applications in Fennoscandia. *Journal of Geodynamics*, *146*, 101845. <https://doi.org/10.1016/j.jog.2021.101845>
- King, M. A., Altamimi, Z., Boehm, J., Bos, M., Dach, R., Elosegui, P., et al. (2010). Improved constraints on models of glacial isostatic adjustment: A review of the contribution of ground-based geodetic Observations. *Surveys in Geophysics*, *31*(5), 465–507. <https://doi.org/10.1007/s10712-010-9100-4>
- Klemann, V., Martinec, Z., & Ivins, E. R. (2008). Glacial isostasy and plate motion. *Journal of Geodynamics*, *46*(3–5), 95–103. <https://doi.org/10.1016/j.jog.2008.04.005>
- Klemann, V., & Wolf, D. (1998). Modelling of stresses in the Fennoscandian lithosphere induced by Pleistocene glaciations. *Tectonophysics*, *294*(3–4), 291–303. [https://doi.org/10.1016/s0040-1951\(98\)00107-3](https://doi.org/10.1016/s0040-1951(98)00107-3)
- Klemann, V., Wu, P., & Wolf, D. (2003). Compressible viscoelasticity: Stability of solutions for homogeneous plane-Earth models. *Geophysical Journal International*, *153*(3), 569–585. <https://doi.org/10.1046/j.1365-246x.2003.01920.x>
- Lagerbäck, R. (1992). Dating of late quaternary faulting in northern Sweden. *Journal of the Geological Society*, *149*(2), 285–291. <https://doi.org/10.1144/gsjgs.149.2.0285>
- Lagerbäck, R., Sundh, M., & undersökning, S. g. (2008). *Early Holocene faulting and paleoseismicity in northern Sweden*. Geological Survey of Sweden. Retrieved from <https://books.google.se/books?id=DqI9PgAACAIA>
- Lambeck, K., & Purcell, A. (2003). *Glacial rebound and crustal stress in Finland*. The Australian National University.
- Lambeck, K., Purcell, A., Zhao, J., & Svensson, N. O. (2010). The Scandinavian ice sheet: From MIS 4 to the end of the last glacial maximum. *Boreas*, *39*(2), 410–435. <https://doi.org/10.1111/j.1502-3885.2010.00140.x>
- Lambeck, K., Purcell, A., & Zhao, S. (2017). The North American Late Wisconsin ice sheet and mantle viscosity from glacial rebound analyses. *Quaternary Science Reviews*, *158*, 172–210. <https://doi.org/10.1016/j.quascirev.2016.11.033>
- Lane, T. P., Paasche, Ø., Kvisvik, B., Adamson, K. R., Rodés, Á., Patton, H., et al. (2020). Elevation changes of the Fennoscandian ice sheet interior during the last deglaciation. *Geophysical Research Letters*, *47*(14), e2020GL088796. <https://doi.org/10.1029/2020GL088796>
- Lecavalier, B. S., Milne, G. A., Simpson, M. J. R., Wake, L., Huybrechts, P., Tarasov, L., et al. (2014). A model of Greenland ice sheet deglaciation constrained by observations of relative sea level and ice extent. *Quaternary Science Reviews*, *102*, 54–84. <https://doi.org/10.1016/j.quascirev.2014.07.018>
- Lindblom, E., Lund, B., Tryggvason, A., Uski, M., Böldvarsson, R., Juhlin, C., & Roberts, R. (2015). Microearthquakes illuminate the deep structure of the endglacial Pärvie fault, northern Sweden. *Geophysical Journal International*, *201*(3), 1704–1716. <https://doi.org/10.1093/gji/ggv112>
- Løvteit, I. F., Fjeldskaar, W., & Sydnes, M. (2019). Tilting and flexural stresses in Basins due to glaciations—An example from the Barents Sea. *Geosciences*, *9*(11), 474. <https://doi.org/10.3390/GEOSCIENCES9110474>
- Lund, B., & Schmidt, P. (2011). Stress evolution and fault stability at Olkiluoto during the Weichselian glaciation.
- Lund, B., Schmidt, P., & Hieronymus, C. (2009). *Stress evolution and fault stability during the Weichselian glacial cycle*. Waste Management.
- MacLean, B., Falconer, R. K. H., & Levy, E. M. (1981). Geological, geophysical and chemical Evidence for natural seepage of petroleum off the northeast coast of Baffin island. *Bulletin of Canadian Petroleum Geology*, *29*(1), 75–95. <https://doi.org/10.35767/gscpgbull.29.1.075>
- Mau, S., Römer, M., Torres, M. E., Bussmann, I., Pape, T., Damm, E., et al. (2017). Widespread methane seepage along the continental margin off Svalbard - From Bjørnøya to Kongsfjorden. *Scientific Reports*, *7*(1), 1–13. <https://doi.org/10.1038/srep42997>
- Mavko, G., Mukerji, T., & Dvorkin, J. (2009). *The rock physics handbook: Tools for seismic analysis of porous media* (2nd ed.). Cambridge University Press. <https://doi.org/10.1017/CBO9780511626753>
- Minakov, A. (2018). Late Cenozoic lithosphere dynamics in Svalbard: Interplay of glaciation, seafloor spreading and mantle convection. *Journal of Geodynamics*, *122*, 1–16. <https://doi.org/10.1016/j.jog.2018.09.009>
- Mitrovica, J. X., & Milne, G. A. (2003). On post-glacial sea level: I. General theory. *Geophysical Journal International*, *154*(2), 253–267. <https://doi.org/10.1046/j.1365-246X.2003.01942.x>
- Näslund, J.-O. (2010). *Climate and climate-related issues for the safety assessment SR-Site*. Svensk Kärnbränslehantering AB. Swedish Nuclear Fuel and Waste Management Co.
- Nield, G. A., Whitehouse, P. L., van der Wal, W., Blank, B., O'Donnell, J. P., & Stuart, G. W. (2018). The impact of lateral variations in lithospheric thickness on glacial isostatic adjustment in West Antarctica. *Geophysical Journal International*, *214*(2), 811–824. <https://doi.org/10.1093/gji/ggy158>
- Nielsen, T., Laier, T., Kuijpers, A., Rasmussen, T. L., Mikkelsen, N. E., & Nørgård-Pedersen, N. (2014). Fluid flow and methane occurrences in the Disko Bugt area offshore west Greenland: Indications for gas hydrates? *Geo-Marine Letters*, *34*(6), 511–523. <https://doi.org/10.1007/s00367-014-0382-2>
- Olivieri, M., & Spada, G. (2015). Ice melting and earthquake stress in Greenland. *Polar Science*, *9*(1), 94–106. <https://doi.org/10.1016/j.polar.2014.09.004>
- Ostani, I., Anka, Z., di Primio, R., & Bernal, A. (2012). Identification of a large Upper Cretaceous polygonal fault network in the Hammerfest basin: Implications on the reactivation of regional faulting and gas leakage dynamics, SW Barents Sea. *Marine Geology*, *332–334*, 109–125. <https://doi.org/10.1016/j.margeo.2012.03.005>
- Patton, H., Hubbard, A., Andreassen, K., Auriac, A., Whitehouse, P. L., Stroeven, A. P., et al. (2017). Deglaciation of the Eurasian ice sheet complex. *Quaternary Science Reviews*, *169*, 148–172. <https://doi.org/10.1016/j.quascirev.2017.05.019>

- Patton, H., Hubbard, A., Andreassen, K., Winsborrow, M., & Stroeven, A. P. (2016). The build-up, configuration, and dynamical sensitivity of the Eurasian ice-sheet complex to Late Weichselian climatic and oceanic forcing. *Quaternary Science Reviews*, *153*, 97–121. <https://doi.org/10.1016/j.quascirev.2016.10.009>
- Peltier, W. R., Argus, D. F., & Drummond, R. (2015). Space geodesy constrains ice age terminal deglaciation: The global ICE-6G-C (VM5a) model. *Journal of Geophysical Research: Solid Earth*, *120*(1), 450–487. <https://doi.org/10.1002/2014JB011176>
- Plaza-Faverola, A., Bünz, S., Johnson, J. E., Chand, S., Knies, J., Mienert, J., & Franek, P. (2015). Role of tectonic stress in seepage evolution along the gas hydrate-charged Vestnesa Ridge, Fram Strait. *Geophysical Research Letters*, *42*(3), 733–742. <https://doi.org/10.1002/2014GL062474>
- Plaza-Faverola, A., Bünz, S., & Mienert, J. (2011). Repeated fluid expulsion through sub-seabed chimneys offshore Norway in response to glacial cycles. *Earth and Planetary Science Letters*, *305*(3–4), 297–308. <https://doi.org/10.1016/j.epsl.2011.03.001>
- Plaza-Faverola, A., & Keiding, M. (2019). Correlation between tectonic stress regimes and methane seepage on the Western Svalbard margin. *Solid Earth*, *10*(1), 79–94. <https://doi.org/10.5194/se-10-79-2019>
- Plaza-Faverola, A., Vadakkepuliambatta, S., Hong, W. L., Mienert, J., Bünz, S., Chand, S., & Greinert, J. (2017). Bottom-simulating reflector dynamics at Arctic thermogenic gas provinces: An example from Vestnesa Ridge, offshore west Svalbard. *Journal of Geophysical Research: Solid Earth*, *122*(6), 4089–4105. <https://doi.org/10.1002/2016JB013761>
- Portillo-Ramos, R. C., Cruz, A. P. S., Barbosa, C. F., Rathburn, A. E., Mulitza, S., Venancio, I. M., et al. (2018). Methane release from the southern Brazilian margin during the last glacial. *Scientific Reports*, *8*(1), 5948. <https://doi.org/10.1038/s41598-018-24420-0>
- Portnov, A., Vadakkepuliambatta, S., Mienert, J., & Hubbard, A. (2016). Ice-sheet-driven methane storage and release in the Arctic. *Nature Communications*, *7*(1), 10314. <https://doi.org/10.1038/ncomms10314>
- Punshon, S., Azetsu-Scott, K., & Lee, C. M. (2014). On the distribution of dissolved methane in Davis strait, North Atlantic Ocean. *Marine Chemistry*, *161*, 20–25. <https://doi.org/10.1016/j.marchem.2014.02.004>
- Ramachandran, H., Plaza-Faverola, A., & Daigle, H. (2022). Impact of gas Saturation and gas Column height at the base of the gas hydrate stability zone on fracturing and seepage at Vestnesa ridge, west-Svalbard margin. *Energies*, *15*(9), 3156. <https://doi.org/10.3390/en15093156>
- Rogozhina, I., Petrunin, A. G., Vaughan, A. P. M., Steinberger, B., Johnson, J. V., Kaban, M. K., et al. (2016). Melting at the base of the Greenland ice sheet explained by Iceland hotspot history. *Nature Geoscience*, *9*(5), 366–369. <https://doi.org/10.1038/ngeo2689>
- Ruppel, C. D., & Kessler, J. D. (2017). The interaction of climate change and methane hydrates. *Reviews of Geophysics*, *55*(1), 126–168. <https://doi.org/10.1002/2016rg000534>
- Schiffer, C., Tegner, C., Schaeffer, A. J., Pease, V., & Nielsen, S. B. (2018). High Arctic geopotential stress field and implications for geodynamic evolution. *Geological Society Special Publication*, *460*(1), 441–465. <https://doi.org/10.1144/SP460.6>
- Schmidt, P., Lund, B., & Hieronymus, C. (2012). Implementation of the glacial rebound prestress advection correction in general-purpose finite element analysis software: Springs versus foundations. *Computers & Geosciences*, *40*, 97–106. <https://doi.org/10.1016/j.cageo.2011.07.017>
- Schmidt, P., Lund, B., Hieronymus, C., MacLennan, J., Árnadóttir, T., & Pagli, C. (2013). Effects of present-day deglaciation in Iceland on mantle melt production rates. *Journal of Geophysical Research: Solid Earth*, *118*(7), 3366–3379. <https://doi.org/10.1002/jgrb.50273>
- Schmidt, P., Lund, B., Näslund, J.-O., & Fastook, J. (2014). Comparing a thermo-mechanical Weichselian ice sheet reconstruction to reconstructions based on the sea level equation: Aspects of ice configurations and glacial isostatic adjustment. *Solid Earth*, *5*(1), 371–388. <https://doi.org/10.5194/se-5-371-2014>
- Schneider, A., Panieri, G., Lepland, A., Consolaro, C., Crémière, A., Forwick, M., et al. (2018). Methane seepage at Vestnesa ridge (NW Svalbard) since the last glacial maximum. *Quaternary Science Reviews*, *193*, 98–117. <https://doi.org/10.1016/j.quascirev.2018.06.006>
- Schotman, H. H. A., Wu, P., & Vermeersen, L. L. A. (2008). Regional perturbations in a global background model of glacial isostasy. *Physics of the Earth and Planetary Interiors*, *171*(1–4), 323–335. <https://doi.org/10.1016/j.pepi.2008.02.010>
- Selway, K., Smirnov, M. Y., Beka, T., O'Donnell, J. P., Minakov, A., Senger, K., et al. (2020). Magnetotelluric constraints on the temperature, composition, partial melt content, and viscosity of the upper mantle beneath Svalbard. *Geochemistry, Geophysics, Geosystems*, *21*(5), e2020GC008985. <https://doi.org/10.1029/2020GC008985>
- Siegert, M. J., & Dowdeswell, J. A. (2004). Numerical reconstructions of the Eurasian ice sheet and climate during the late Weichselian. *Quaternary Science Reviews*, *23*(11–13), 1273–1283. <https://doi.org/10.1016/j.quascirev.2003.12.010>
- Smith, A. J., Mienert, J., Bünz, S., & Greinert, J. (2014). Thermogenic methane injection via bubble transport into the upper Arctic Ocean from the hydrate-charged Vestnesa ridge, Svalbard. *Geochemistry, Geophysics, Geosystems*, *15*(5), 1945–1959. <https://doi.org/10.1002/2013gc005179>
- Spada, G., Barletta, V. R., Klemann, V., Riva, R. E. M., Martinec, Z., Gasperini, P., et al. (2011). A benchmark study for glacial isostatic adjustment codes. *Geophysical Journal International*, *185*(1), 106–132. <https://doi.org/10.1111/j.1365-246X.2011.04952.x>
- Steffen, H., Olesen, O., & Sutinen, R. (2021). *Glacially-triggered faulting*. In H. Steffen, O. Olesen, & R. Sutinen (Eds.). Cambridge University Press. <https://doi.org/10.1017/9781108779906>
- Steffen, R., Steffen, H., Weiss, R., Lecavalier, B. S., Milne, G. A., Woodroffe, S. A., & Bennike, O. (2020). Early Holocene Greenland-ice mass loss likely triggered earthquakes and tsunamis. *Earth and Planetary Science Letters*, *546*, 116443. <https://doi.org/10.1016/j.epsl.2020.116443>
- Steffen, R., Steffen, H., Wu, P., & Eaton, D. W. (2014). Stress and fault parameters affecting fault slip magnitude and activation time during a glacial cycle. *Tectonics*, *33*(7), 1461–1476. <https://doi.org/10.1002/2013tc003450>
- Tesauro, M., Kaban, M. K., & Cloetingh, S. A. P. L. (2013). Global model for the lithospheric strength and effective elastic thickness. *Tectonophysics*, *602*, 78–86. <https://doi.org/10.1016/j.tecto.2013.01.006>
- Waage, M., Bünz, S., Landrø, M., Plaza-Faverola, A., & Waghorn, K. A. (2018). Repeatability of high-resolution 3D seismic data. *Repeatability of High-Resolution 3D Seismic Data*, *84*(1), B75–B94. <https://doi.org/10.1190/geo2018-0099.1>
- Wallmann, K., Drews, M., Aloisi, G., & Bohrmann, G. (2006). Methane discharge into the Black Sea and the global ocean via fluid flow through submarine mud volcanoes. *Earth and Planetary Science Letters*, *248*(1–2), 545–560. <https://doi.org/10.1016/j.epsl.2006.06.026>
- Winsborrow, M., Andreassen, K., Hubbard, A., Plaza-Faverola, A., Gudlaugsson, E., & Patton, H. (2016). Regulation of ice stream flow through subglacial formation of gas hydrates. *Nature Geoscience*, *9*(5), 370–374. <https://doi.org/10.1038/ngeo2696>
- Wu, P. (1992a). Deformation of an incompressible viscoelastic flat Earth with powerlaw creep: A finite element approach. *Geophysical Journal International*, *108*(1), 35–51. <https://doi.org/10.1111/j.1365-246X.1992.tb00837.x>
- Wu, P. (1992b). Viscoelastic versus viscous deformation and the advection of pre-stress. *Geophysical Journal International*, *108*(1), 136–142. <https://doi.org/10.1111/j.1365-246X.1992.tb00844.x>
- Wu, P. (2004). Using commercial finite element packages for the study of Earth deformations, sea levels and the state of stress. *Geophysical Journal International*, *158*(2), 401–408. <https://doi.org/10.1111/j.1365-246X.2004.02338.x>
- Wu, P., & Hasegawa, H. S. (1996). Induced stresses and fault potential in eastern Canada due to a realistic load: A preliminary analysis. *Geophysical Journal International*, *127*(1), 215–229.
- Wu, P., Johnston, P., & Lambeck, K. (1999). Postglacial rebound and fault instability in Fennoscandia. *Geophysical Journal International*, *139*(3), 657–670. <https://doi.org/10.1046/j.1365-246x.1999.00963.x>